

DTIC COPY

AFRL-VS-HA-TR-2005-1030

SEISMOLOGICAL AND LITHOSPHERIC STUDIES OF THE LIBYA REGION

**W. A. Brown
D. I. Doser
T. F. VanDeMark
A. A. Velasco
G. R. Keller**

**University of Texas at El Paso
500 W. University Avenue
El Paso, TX 79968-0697**

December 2004

Final Report


APPROVED FOR PUBLIC RELEASE; DISTRIBUTION UNLIMITED.



**AIR FORCE RESEARCH LABORATORY
Space Vehicles Directorate
29 Randolph Rd
AIR FORCE MATERIEL COMMAND
Hanscom AFB, MA 01731-3010**

This technical report has been reviewed and is approved for publication.


ROBERT RAISTRICK
Contract Manager


ROBERT BELAND
Branch Chief

This document has been reviewed by the ESC Public Affairs Office and has been approved for release to the National Technical Information Service (NTIS).

Qualified requestors may obtain additional copies from the Defense Technical Information Center (DTIC). All others should apply to the NTIS.

If your address has changed, if you wish to be removed from the mailing list, or if the addressee is no longer employed by your organization, please notify AFRL/VSIM, 29 Randolph Rd., Hanscom AFB, MA 01731-3010. This will assist us in maintaining a current mailing list.

Do not return copies of this report unless contractual obligations or notices on a specific document require that it be returned.

REPORT DOCUMENTATION PAGEForm Approved
OMB No. 0704-0188

Public reporting burden for this collection of information is estimated to average 1 hour per response, including the time for reviewing instructions, searching existing data sources, gathering and maintaining the data needed, and completing and reviewing this collection of information. Send comments regarding this burden estimate or any other aspect of this collection of information, including suggestions for reducing this burden to Department of Defense, Washington Headquarters Services, Directorate for Information Operations and Reports (0704-0188), 1215 Jefferson Davis Highway, Suite 1204, Arlington, VA 22202-4302. Respondents should be aware that notwithstanding any other provision of law, no person shall be subject to any penalty for failing to comply with a collection of information if it does not display a currently valid OMB control number. **PLEASE DO NOT RETURN YOUR FORM TO THE ABOVE ADDRESS.**

1. REPORT DATE (DD-MM-YYYY) 31-12-2004		2. REPORT TYPE Final		3. DATES COVERED (From - To) 1 Sep 2001 to 31 Dec 2004	
4. TITLE AND SUBTITLE Seismological and Lithospheric Studies of the Libya Region				5a. CONTRACT NUMBER DTRA01-01-C-0058	
				5b. GRANT NUMBER	
				5c. PROGRAM ELEMENT NUMBER	
6. AUTHOR(S) W. A. Brown, D. I. Doser, T. F. VanDeMark, A. A. Velasco and G. R. Keller				5d. PROJECT NUMBER DTRA	
				5e. TASK NUMBER OT	
				5f. WORK UNIT NUMBER A1	
7. PERFORMING ORGANIZATION NAME(S) AND ADDRESS(ES) University of Texas at El Paso 500 W. University Avenue El Paso, TX 79968-0697				8. PERFORMING ORGANIZATION REPORT NUMBER	
9. SPONSORING / MONITORING AGENCY NAME(S) AND ADDRESS(ES) Air Force Research Laboratory 29 Randolph Road Hanscom AFB, MA 01731-3010 Contract Manager: R. Raistrick AFRL/VSBYE				10. SPONSOR/MONITOR'S ACRONYM(S) AFRL/VSBYE	
				11. SPONSOR/MONITOR'S REPORT NUMBER(S) AFRL-VS-HA-TR-2005-1030	
12. DISTRIBUTION / AVAILABILITY STATEMENT Approved for Public Release; Distribution Unlimited.					
13. SUPPLEMENTARY NOTE					
14. ABSTRACT This report constitutes an integrated geophysical investigation of the lithospheric structure in the region of Libya. It is separated into five sections. The final four sections represent papers that will be submitted to different scientific journals for publication. In the first part of the study, we utilized a seamless mosaicking approach based on the commercial Environment for Visualizing Images (ENVI) software package to create mosaics of two geologically interesting portions of Libya. For the second portion of the research, we made use of over 6,000 free air corrected gravity data in conjunction with other geological and geophysical data to develop a 3D density model for northern Libya. We then used the Nafe-Drake relationship along with other geological data to convert the 3D density model to a 3D velocity model (LIBYA3D) for the region. Two earthquakes having source receiver paths sampling much of the modeled area were used to perform 1D and 1.5D validation tests, and the results were compared to those from previous studies. In the final part of this report, we utilize a 3-D geophysical model, "LIBYA3D," in the context of regional discrimination to investigate small to moderate size natural events (mb 3.7 - 5.7) in the Libyan region occurring from May 1990 to May 2000. Observations of <i>Pn</i> and <i>Sn</i> energy at varying frequency ranges (0.5 - 8 Hz) and propagation paths recorded by broadband instrumentation led us to investigate the attenuation affects of the geologic structure of the Libyan region and the adjacent Mediterranean Sea.					
15. SUBJECT TERMS Seismic velocity Seismic propagation Seismic sources					
16. SECURITY CLASSIFICATION OF:			17. LIMITATION OF ABSTRACT SAR	18. NUMBER OF PAGES	19a. NAME OF RESPONSIBLE PERSON Robert J. Raistrick
a. REPORT UNCLAS	b. ABSTRACT UNCLAS	c. THIS PAGE UNCLAS			19b. TELEPHONE NUMBER (include area code) 781-377-3726

Abstract

This report constitutes an integrated geophysical investigation of the lithospheric structure in the region of Libya. It is separated into five sections. The final four sections represent papers that will be submitted to different scientific journals for publication. In the first part of the study, we utilized a seamless mosaicking approach based on the commercial Environment for Visualizing Images (ENVI) software package to create mosaics of two geologically interesting portions of Libya. In this study we present a step by step method of mosaicking Landsat 4 satellite images. Firstly, we performed histogram matching to give images the same color scale, then we used a cutline feathering technique to blend suture areas and finally we overlaid the images to form the two mosaics. The resulting mosaics were then combined with structural features and the seismicity map of the area. The resulting mosaics were proven to be useful in identifying recently active faults and shows great potential for verification of other faults and in natural hazard assessment.

For the second portion of my research, we made use of over 6,000 Free Air corrected gravity data in conjunction with other geological and geophysical data to develop a 3D density model for northern Libya. We used a gravity modeling program (SURFgrav) to develop the 3D density model by manipulating it to accurately predict large areas of Free Air anomaly shown in the data. The residual gravity anomaly values were calculated by subtracting predicted Free Air anomaly from the observed Free Air anomaly. The results were satisfactory for uplifted areas of Libya while there were significant mismatches in basin areas. The density model was iterated and used as a starting model for the final portion of the study.

We then used the Nafe-Drake relationship along with other geological data to convert the 3D density model to a 3D velocity model (LIBYA3D) for the region. Two earthquakes having source receiver paths sampling much of the modeled area were used to perform 1D and 1.5D validation tests, and the results were compared to those from previous studies. The results also showed that the new 3D velocity model is valid and superior to the global model. However, until there is sufficient earthquake data acquired, and we are able to perform 2D and 3D modeling we may not be able to see the true improvement of LIBYA3D as compared to the other regional models.

In the final part of this report, we utilize a 3-D geophysical model, "LIBYA3D," in the context of regional discrimination to investigate small to moderate size natural events (m_b 3.7 – 5.7) in the Libyan region occurring from May 1990 to May 2000.

Observations of P_n and S_n energy at varying frequency ranges (0.5 – 8 Hz) and propagation paths recorded by broadband instrumentation led us to investigate the attenuation affects of the geologic structure of the Libyan region and the adjacent Mediterranean Sea. We perform multi-frequency analysis to discern which frequencies have the optimum signal to noise ratio (SNR) for these regional phases. P_n and S_n SNR show stronger amplitudes at higher frequencies (4 – 8 Hz) along propagation paths where continental crust is limited. Conversely, we only observe strong P_n and S_n amplitudes at lower frequencies (0.5 – 4 Hz) along propagation paths where continental crust is prevalent. We utilize LIBYA3D to develop relationships in our data as a function of crustal path, Moho variance, and volume.

Table of Contents

Abstract.....	iii
Table of Contents	iv
Table of Figures.....	vi
List of Tables	ix
Acknowledgements	ix
Section 1	1
Executive Summary	1
Section 2	2
A SEAMLESS MOSAICKING OF LANDSAT IV IMAGES OF NORTHERN LIBYA AND ITS APPLICATIONS.....	2
Summary.....	2
Introduction.....	2
Study Areas and Data	3
Seamless Mosaicking Technology.....	4
Histogram Matching Based on Overlay Parts.....	4
Feathering Technique to Blend Suture Areas	5
Ordering overlain Images	7
Results and Summary.....	8
Conclusions.....	10
Section 3	12
THE USE OF FREE AIR GRAVITY DATA TO CONSTRUCT A 3D DENSITY MODEL FOR THE REGION OF LIBYA	12
Summary.....	12
Introduction.....	12
Geology.....	13
Previous work.....	16
“SURFGRAV”	19
Computation Techniques Used in SURFGRAV.....	21
Gravity Data	21
Construction of the Density Model.....	22
Topography	22
Layers.....	22
Results/Discussion	27
Conclusions.....	31
Section 4	32
DEVELOPMENT AND VALIDATION OF A 3D VELOCITY MODEL FOR THE LIBYA REGION	32
Summary.....	32
Introduction.....	32
Existing Geophysical Work.....	34
Geophysical Model Development	37
1D Validation of 3D Velocity Model.....	42
Error Analysis	44

Conclusions	47
Section 5	48
ANALYSIS OF HIGH FREQUENCY PROPAGATION IN THE LIBYAN REGION UTILIZING A 3-D GEOPHYSICAL MODEL	48
Summary	48
Introduction	48
LIBYA3D Velocity Model	49
Regional Seismic Data	51
Application of LIBYA3D	54
Discussion	56
Conclusions	56
REFERENCES	58

Table of Figures

Figure 1. Basemap of the study area showing the area covered by the remotely sensed Landsat IV images. The labels indicate the path/row of the images. The red lines indicate faults cutting rocks of Mesozoic age and younger, while the black lines indicate faults cutting rocks of Precambrian age.....	3
Figure 2. The overlapping parts of the two images are marked as ROIs (red on left image and green on the right image). The left image is path/row of 184/38 and the right image is 183/38. It is clear that the right image is significantly brighter than the left image.	5
Figure 3. Illustration of the histogram matching method. Notes: The histogram of the ROI in 183/38, the base histogram, is used to match the histogram of ROI in 184/38. The histogram for image 183/38 remains unchanged, but for image 184/38, the output histogram more closely resembles the output histogram in image 183/38.	6
Figure 4. Images after histogram matching.	7
Figure 5. Final mosaicked image for the northeastern portion of Libya.	8
Figure 6. This figure shows the two mosaicked area overlain by mapped faults in Libya. The blue faults are faults that cut Precambrian and younger rocks (Goudarzi et al., 1978), the red faults cut only Mesozoic (Goudarzi et al., 1978) and younger rocks, and the magenta faults are other mapped faults of unknown age in the region (Hearn et al., 2001). The red dots show the seismicity of the region (1975-2004) earthquakes are of magnitude 3.5 and above (NEIC PDE catalog) (see Table 1).	9
Figure 7. This figure shows the nine mosaicked images for northwestern Libya. Part a) shows the image after mosaicking and part b) shows the image overlain by seismicity, mapped faults and assumed unmapped faults (green lines).	10
Figure 8. Map of Libya showing the spatial extent of basins and uplifts occurring in Libya (Based on Hearn, 2001).	14
Figure 9. Generalized geologic map of Libya and adjacent areas.	15
Figure 10. Map of North Africa showing the location of gravity stations and profiles constructed by Dial (1998).	17
Figure 11. Dial's 1998 model for gravity profile 1 (see Figure 10 for location of profile). The model extends for 2620 km from southern Algeria to northern Egypt (Dial, 1998).	18
Figure 12. Flow chart for processing and modeling 3D gravity.	20
Figure 13. Map of Libya showing the locations of the gravity readings used in this study.	22
Figure 14. Vertically exaggerated DEM of Libya. The minimum curvature technique was used in the gridding. The gridding was done at 30 sec. spacing. Data used to create the DEM was obtained from the GTOPO30 database. Elevation is in meters.	23
Figure 15. Simplified density map of the surface geology of Libya.	25
Figure 16. Illustration of the arrangement of the layers used in the density model. The wavy lines represent the irregular surfaces that were obtained from maps and other sources. The upper surface of the lower crust is set at 19 km based on previous studies. The base of the model is at 50 km.	26
Figure 17. Isopach map of the upper layer of the model. This layer combines the Cenozoic and Mesozoic layers. Basins appear as domes since the layer is thicker in areas where the basins are filled.....	28

Figure 18. Calculated gravitational contribution of the uppermost layer of the model. Data are unavailable south of latitude 26N, hence the grid is truncated. Note the similarities in where the highs and lows occur compared with those of the isopach map (Figure 17).	29
Figure 19. Sum of the gravitational contribution of the layers used in the model. The contribution from the Mantle had the most significant impact on the results, as it is the thickest and most dense layer.	30
Figure 20. Map showing the residual Free Air gravity distribution. The residual gravity values were calculated by subtracting the observed Free Air gravity from the calculated Free Air values. Positive residual values represent areas where the Free Air gravity was over estimated.	31
Figure 21. Map showing the residual Free Air gravity distribution. The residual gravity values were calculated by subtracting the observed Free Air gravity from the calculated Free Air values. Positive residual values represent areas where the Free Air gravity was overestimated (from Brown, 2004).	33
Figure 22. Seismicity map of the Libya region showing earthquakes as red diamonds, stations as blue triangles and the multicolored lines represent source receiver paths. Blue lines show source receiver pathways that were suitable for testing our model. Focal mechanisms indicate the primary events used to validate LIBYA3D.	34
Figure 23. Epicenters of Libyan earthquakes (1931 – 1994). Relocated earthquakes are denoted by solid triangles (from Suleiman and Doser, 1995).	36
Figure 24. Average 1D velocity model beneath Libya. The wavy lines indicate surfaces that were digitized from data. A uniform depth of 19 km was assumed for the top of the lower crust. Density values are given in g/cc.	38
Figure 25. The velocity/density model resulting from our study. Dashed lines represent the IASPEI91 model.	39
Figure 26. Slices through the LIBYA3D velocity model at (a) 0 km depth, (b) 1 km depth, and (c) 3 km depth. Blue represents areas with a velocity (V_p) of 5.45 km/s and (V_s) of 3.1 km/s. Green represents areas of velocity (V_p) of 5.53 km/s and (V_s) of 3.2km/s. Red represents areas of velocity (V_p) of 7.16km/s and (V_s) of 4.04 km/s.	41
Figure 27. Unfiltered seismogram of a) event 921012 and b) event 980528 recorded at TAM. The arrival time of the P-wave as predicted by our 1D model (red lines) and as well as the predicted S-wave arrival time (blue lines).	43
Figure 28. Waveform comparison between synthetic and data for events 921012 and 980528 used in the validation study. The seismograms were recorded at TAM. A band pass (10 – 100s) Butterworth filter has been applied to the data and the synthetic seismograms.	45
Figure 29. Plots of the results of our 1.5D error analysis exercise. The seismograms were recorded at TAM.	46
Figure 30. Map of study areas show earthquakes as black diamonds, stations as black triangles, and grey great circle arcs represent source-receiver paths.	49
Figure 31. A portion of the LIBYA3D Moho boundary DEM used in our study showing crustal thickness under Libya, note the thinning crust to the north as Libya approaches the Mediterranean Sea.	51
Figure 32. Vertical component multi-frequency bandpassed seismogram of the 02 February 1991 event recorded at KEG. Note that SNR increases at the higher frequency	

ranges. This is a good example that led us to question what path effects were responsible for the observed high frequency propagation.	52
Figure 33. Vertical component multi-frequency seismograms from the 990331 and 920701 events. Notice the different high-frequency propagation when comparing IDI and KEG to TAM. Also note that even though the receiver distance is greater to KEG than to TAM for 920701 a distinguishable signal is still present from 4 to 8 Hz at KEG.....	53
Figure 34. SNR-Frequency diagrams show trends in station-frequency dependence, note the unusual high frequency propagation displayed at KEG accompanied by the expected high frequency attenuation at TAM.....	54
Figure 35. Cross-spectral value plots show a good correlation between the continental crust percentage in the source-receiver path and cross-spectral values at KEG (A & B). Strong correlations are also shown for IDI, TAM, and WDD when compared to crustal volume and continental crust percentage (C & D). Finally, we observe converse trends at KEG when compared to the standard deviation of the Moho depth (E & F).	55

List of Tables

Table 1. List of events occurring in the study region (1975 – 2000). Only events between latitude 18N - 33N and Longitude 25E – 10E are listed in this table. (Source NEIC PDE catalogue).....	11
Table 2. Summarized density assigned to the generalized geology of Libya. Table also shows the age and basic composition of the different units.....	24
Table 3. Layers used in the density model, along with their average thickness, assigned density and the source from which the densities were obtained.....	27
Table 4. Comparison of error analysis results (in amplitudes of meters) of LIBYA3D, IASPEI91 and the Dial Model.	47
Table 5. Earthquake Source Parameters (International Seismic Centre).....	50

Acknowledgements

We wish to thank the Incorporated Research Institutions for Seismology's (IRIS) Data Management Center (DMC) for providing the waveform data used for this study. This work was supported by a grant from the Air Force Research Laboratory (Contract No. DTRA01-01-C-0058).

Section 1

Executive Summary

Our final report is in four parts. Part one is the text of a paper to be submitted for publication entitled "A Seamless Mosaicking of Landsat IV Images of Northern Libya and its Application." In this paper we utilized a seamless mosaicking approach based on the commercial Environment for Visualizing Images (ENVI) software package to create mosaics of two geologically interesting portions of Libya. The resulting mosaics were proven to be useful in identifying recently active faults and show great potential for verification of other faults and in natural hazard assessment.

Part two is the text of a paper to be submitted for publication, entitled "The Use of Free Air Gravity Data to Construct A 3D Density Model for the Region of Libya." In this paper we made use of over 6,000 Free Air corrected gravity data in conjunction with other geological and geophysical data to develop a 3D density model for northern Libya. The results were satisfactory for uplifted areas of Libya while there were significant mismatches in basin areas. The density model was iterated and used as a starting model for the next two portions of the study.

Part three is the text of a paper to be submitted for publication, entitled "Development and Validation of a 3D Velocity Model for the Libya Region." In this paper we used the Nafe-Drake relationship along with other geological data to convert the 3D density model to a 3D velocity model (LIBYA3D) for the region. We use two earthquakes having source receiver paths sampling much of the modeled area to perform 1D and 1.5D validation tests. The results showed that the new 3D velocity model is valid and superior to the global model.

Part four is the text of a paper submitted for publication in the Bulletin of the Seismological Society of America entitled "Analysis of High Frequency Propagation in the Libyan Region Utilizing A 3D Geophysical Model". In this paper we utilize our 3D geophysical model, "LIBYA3D," in the context of regional discrimination to investigate small to moderate size natural events (m_b 3.7 – 5.7) in the Libyan region occurring from May 1990 to May 2000. Observations of Pn and Sn energy at varying frequency ranges (0.5 – 8 Hz) and propagation paths recorded by broadband instrumentation led us to investigate the attenuation effects of the geologic structure of the Libyan region and the adjacent Mediterranean Sea. These empirical observations could be used to aid future explosion discrimination work in the Libyan region if the need arises.

Section 2

A SEAMLESS MOSAICKING OF LANDSAT IV IMAGES OF NORTHERN LIBYA AND ITS APPLICATIONS

Summary

The general goal of mosaicking is to create a single seamless image by aligning a series of overlapping images. The result is a larger image that portrays a large area of interest. In this paper, we utilized a seamless mosaicking approach based on the commercial Environment for Visualizing Images (ENVI) software package to create mosaics of portions of northeastern and northwestern Libya. The mosaics were created from thirteen georeferenced Landsat 4 satellite images. The two areas chosen (NE Libya and NW Libya) are geologically interesting in terms of seismic activity, complex surface geology, and several styles of active faulting. The resulting mosaics have great potential to aid in the verification of previously mapped faults, identification of other unmapped faults, and assessment of natural hazards and risk.

Introduction

Mosaicking is a technique of image processing that was initially used to manually combine aerial photographs. Satellite image mosaicking is the process of digitally combining several individual satellite images so that the boundaries between the original images are not seen. Image mosaicking requires geometric corrections, so that all of the images match in a geographic sense. When transformed to any local coordinate system (e.g. UTM) and then mosaicked, the result is an orthophoto map sheet (Afek and Brand, 1998). The transformation of the images to a local coordinate system (Moik, 1980) is also called orthorectification. For this study, the images to be mosaicked were orthorectified to UTM zone 34.

Image mosaics can be used for different applications such as, construction of virtual environments and virtual travel (Kim et al. 2003, Szeliski 1996, and Szeliski and Shum 1997); for scene stabilization (Hansen et al. 1994, and Irani et al. 1995a, b); and for scene change detection, video compression and video indexing (Irani and Anandan 1998). Here we use it for the purpose of fault identification, verification and natural hazard mapping.

Creating an image mosaic was originally performed using photomechanical devices (Mullen, 1980; Afek, 1998). Creating a mosaic in this manner has always been tedious and incurs considerable room for error. Non digital mosaicking is still in use (e.g., Vickers, 1993). In this paper we propose a step by step digital method of mosaicking. This method is not fully automated but it is a quick and relatively simple technique which will provide a way of creating mosaicking, especially in cases where a remote sensing software is not equipped with a built in automated mosaicking routine.

Mosaicking remotely sensed images for the northern region of Libya will assist in the analysis of structural features in the area. In this paper we utilize a seamless mosaicking technology to create mosaics of northern Libya. First, we performed histogram matching based on the portions of adjacent scenes that overlapped. We then

used a cutline feathering technique to blend the suture areas. Finally, we overlaid the images to form a complete mosaic.

Mosaicking satellite images will provide insight into recent faulting and seismicity in the region. This paper represents part of an effort to better understand the ways in which seismic waves propagate across the Libyan lithosphere so that earthquakes can be discriminated from nuclear testing. The results of this project will be useful to the nuclear monitoring community and anyone interested in locating seismic events within Libya or in modeling the propagation of seismic waves across North Africa.

Study Areas and Data

Northern Libya, situated in the Mediterranean foreland of the African shield, extends over a platform of cratonic basins and includes classic examples of continental rifts and domal uplifts. These basins were active as recently as the Late Tertiary and Holocene (Goudarzi, 1980). Faults with various trends are present in Libya, but the major fault systems trend sub-parallel to the Red Sea. This study is part of a large effort to better understand the lithospheric structure beneath Libya, utilizing the seismic studies as well as satellite imagery to identify recently active faults.

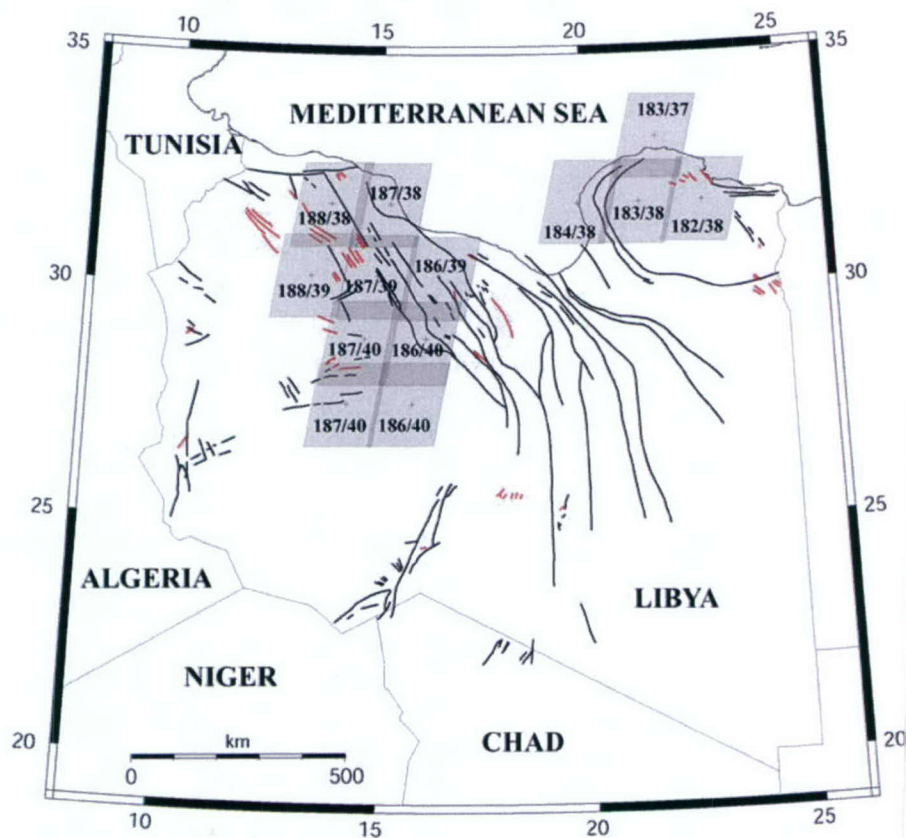


Figure 1. Basemap of the study area showing the area covered by the remotely sensed Landsat IV images. The labels indicate the path/row of the images. The red lines indicate faults cutting rocks of Mesozoic age and younger, while the black lines indicate faults cutting rocks of Precambrian age.

Thirteen remotely sensed Landsat 4 images covering two different regions of Northern Libya were carefully selected for this study (). Four of the images are 182/38 (path/row), 183/38, 184/38 and 183/37, covering a portion of northeastern Libya (Cyrenaica Uplift). This area is the second most seismically active portion of the country and is the site of much recent seismic activity. The geology of this area is mostly composed of Triassic rocks and Quaternary surficial deposits. A few major basement high angle reverse faults are located in the area. The other nine images (186/39, 186/40, 186/41, 187/38, 187/39, 187/40, 187/41, 188/38, and 188/39) cover the northwestern portion of the country. This region is the most seismically active portion of the country, highly faulted, geologically much more complex, and contains a portion of the Hun Graben. The Hun graben trends NW-SE and is a classical example of well-exposed normal block faulting (Suleiman and Doser, 1995). In the northwest area, strike-slip faulting is common with a general northwesterly trend. Analysis of these images will help in identifying the more recently active faults and previously unmapped faults.

In order to best interpret these faults, it is necessary to mosaic the individual images. The mosaicked image will also serve as a base map for overlaying other information such as earthquake locations, which will help interpreters to better understand the relationship between earthquakes and faults.

Seamless Mosaicking Technology

Mosaicking is the art of combining multiple images into a single composite image. It can be used to combine pixel-based images, or as a means for combining georeferenced images into a single image covering a larger geographic area. The seamless mosaicking approach based on the commercial Environment for Visualizing Images (ENVI) software package used in this study was first developed by Xie (2002) and improved in this study. This approach involves three procedures: (histogram matching, outline feathering, and ordering overlain images) that are discussed in turn below.

Histogram Matching Based on Overlay Parts

In order to match two images that will be mosaicked, Step1 is to mark the overlapping parts of the two images as a region of interest (ROI), for example, the images with marked ROIs are shown in Figure 2. Step 2 (Figure 3) is to match the two images by matching the histograms of the two ROIs. The histogram of the image 184/38 is set to stretch type arbitrary, since its output will be modified to resemble the histogram of image 183/38. The output histogram of the base image (183/38) is then dragged and dropped onto the output histogram of image 184/38 and applied. The procedure is repeated twice for the other colors of the RGB color spectra. This gives the overlapping region almost exactly the same grayscale distribution (Figure 4). The improvement of this step compared to other histogram matching is that, instead of matching the entire images, we only match the overlapping areas (ROIs). There is a risk when matching the entire images due to large black areas (DN is 0) outside the image. These large zero value areas significantly impact the distribution of Display Number (DN) value, and then impact the histogram matching. Figure 4 is the result of histogram matching.

Feathering Technique to Blend Suture Areas

After finishing the histogram matching, a cutline feathering technique was used for blending the suture areas. A cutline must be defined using the annotation tool prior to mosaicking, usually along the seam where one desires the mosaicked boundary to be matched. The annotation file must contain a polyline (white line, image 184/38 of) as a cutline that is drawn from edge-to-edge and a symbol (green star) that is placed in the region of the image that will be cut off (). The cutline distance is used to create a linear ramp that averages the two images across that distance from the cutline outwards.

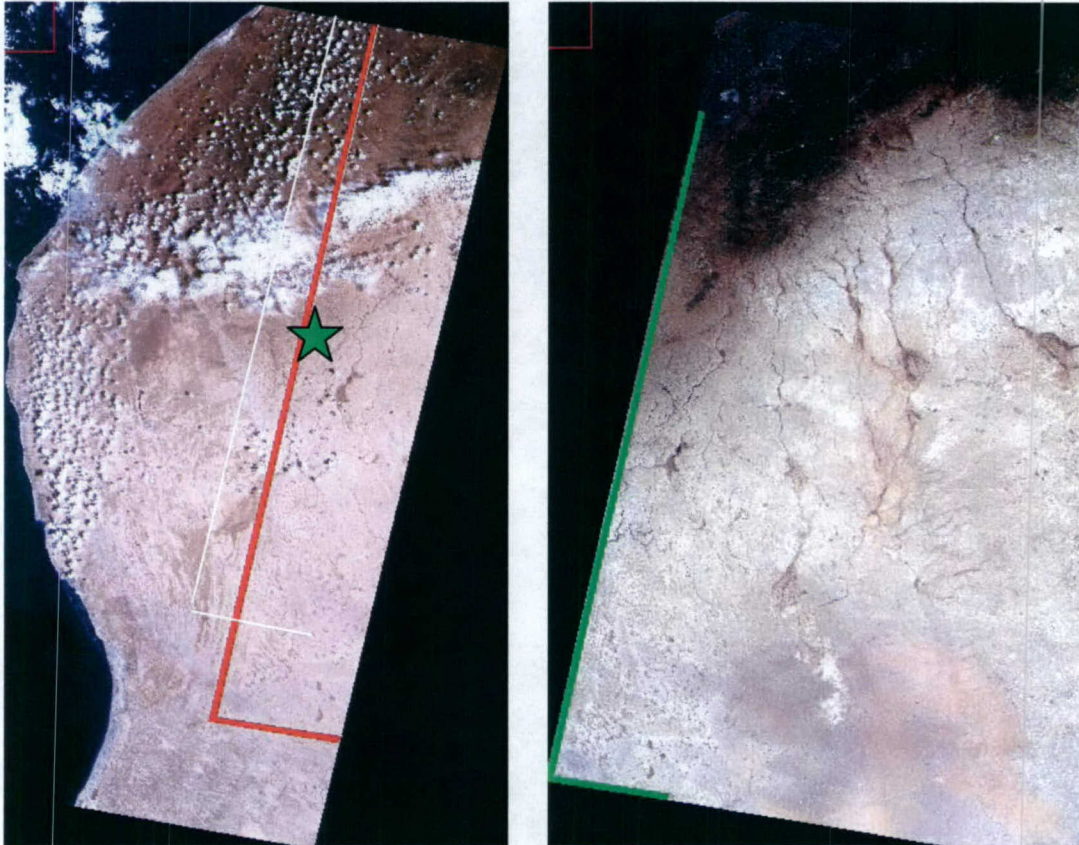


Figure 2. The overlapping parts of the two images are marked as ROIs (red on left image and green on the right image). The left image is path/row of 184/38 and the right image is 183/38. It is clear that the right image is significantly brighter than the left image.

Before Histogram Matching

After Histogram Matching

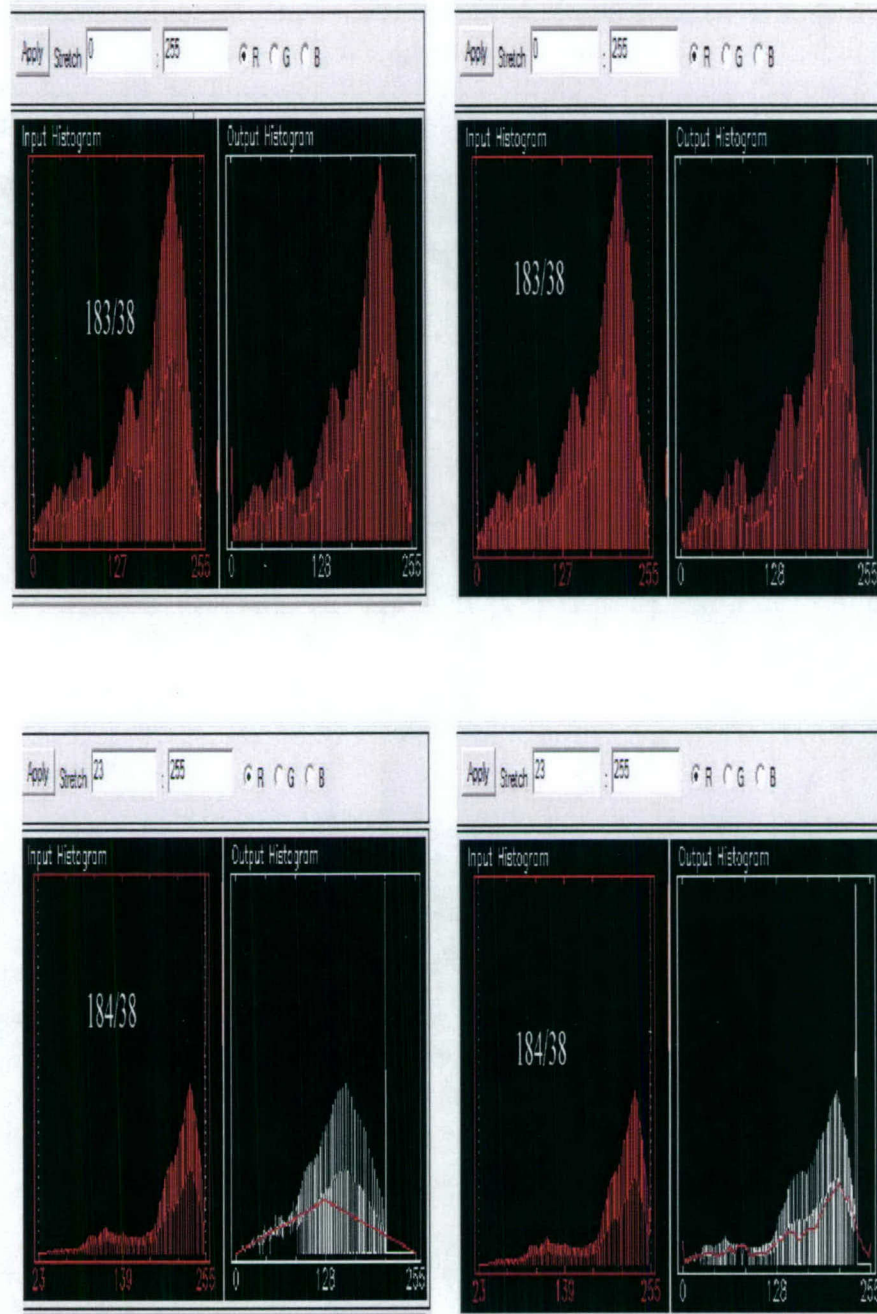


Figure 3. Illustration of the histogram matching method. Notes: The histogram of the ROI in 183/38, the base histogram, is used to match the histogram of ROI in 184/38. The histogram for image 183/38 remains unchanged, but for image 184/38, the output histogram more closely resembles the output histogram in image 183/38.



Figure 4. Images after histogram matching.

Ordering overlain Images

It is important to place the images in a particular order before trying to decide which image will have the cutline and symbol on it. Here are some basic principles that need to be kept in mind:

- 1) The base image will always stay on the bottom, and the other adjacent images that will be cut off while mosaicking will always stay on the top.
- 2) The cutline must be within the bounds of both the images being cut and the base image, otherwise there will be a gap left in the final mosaicked image.
- 3) The cutline needs to be assigned for every two adjacent images, otherwise there will be a seam left along the bounds of the top image because there is a linear ramp area created along a cutline by averaging the two images using a specified cutline distance (300 pixels in our case). If a cutline is not defined along two adjacent images, there will be no calculation along the suture area and a seam will be left along the bounds of the top image.

Results and Summary

Figure 5 shows the final mosaicked image from 4 individual scenes for the northeastern portion of Libya. From this image, we cannot see any visible effects along the seams and color contrast from image to image, which means that this is a good mosaic. In Figure 6 we have overlain mapped Precambrian faults, Mesozoic faults and seismicity of the area over Figure 5. This mosaic clearly indicates the correlation between faults and possible changes in vegetation. It is noteworthy however, that the images depict surface reflectance that is not always related to vegetation. Having the faults overlain on top of the mosaicked image helps to discern what a fault looks like on a satellite image. This helps us in identifying suspect or unmapped faults. We may also be able to determine relative age of some of the faults based on their geomorphic expression and crosscutting relationships with other features. Since the faulting styles exhibited in the Cyrenaica Uplift and the Hun Graben area are so different, we may even be able to identify the styles of some of the unmapped faults based purely on the satellite images.

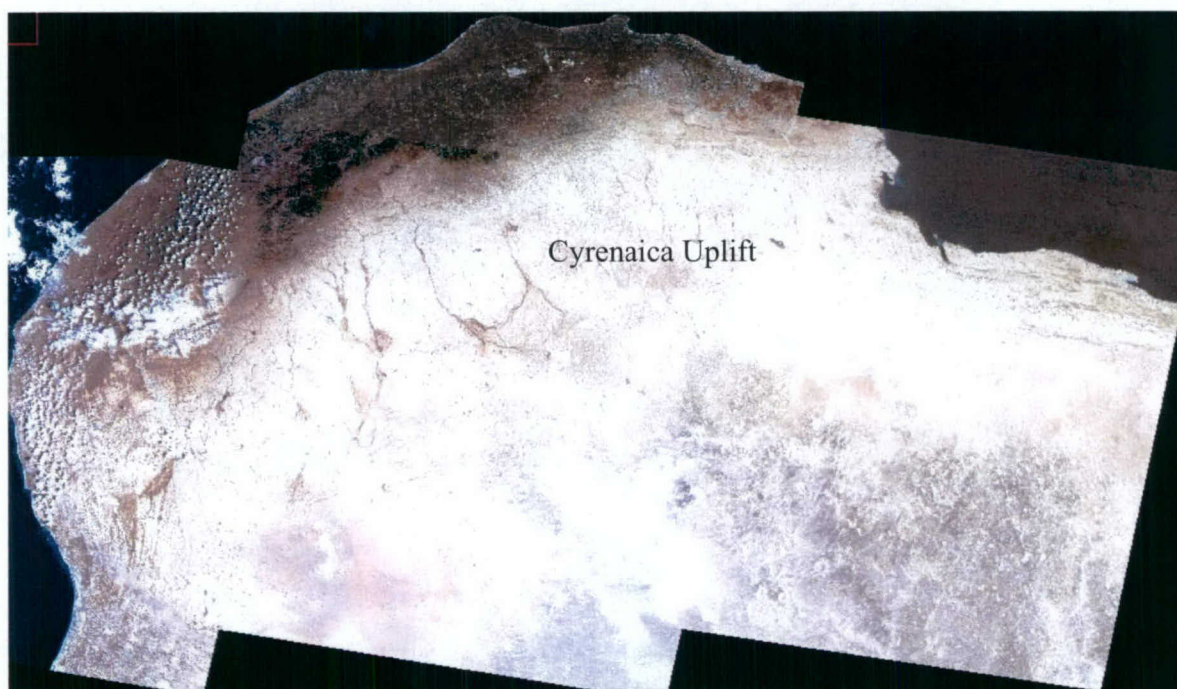


Figure 5. Final mosaicked image for the northeastern portion of Libya.

Another overlay including earthquake locations (Figure 6) may enable us to associate earthquakes with the specific causative faults.

From the mosaicked images several unmapped and probably unknown topographic features have been noted, particularly on the mosaicked image in the northwest region of Libya. The northwest-southeast trending faults that define the flanks of the Hun Graben are clearly seen, but their exact position may be slightly off due to pixel shifting (e.g., Scheik, 2004). Additional active faults can also be seen in the area based on the similarities shown on the mosaicked image to other mapped faults (Figure 7). The topography of the Cyrenaica area has been outlined and can be used to produce more accurate geographical maps of the region, therefore improving our ability to produce geo-hazard zonation maps.

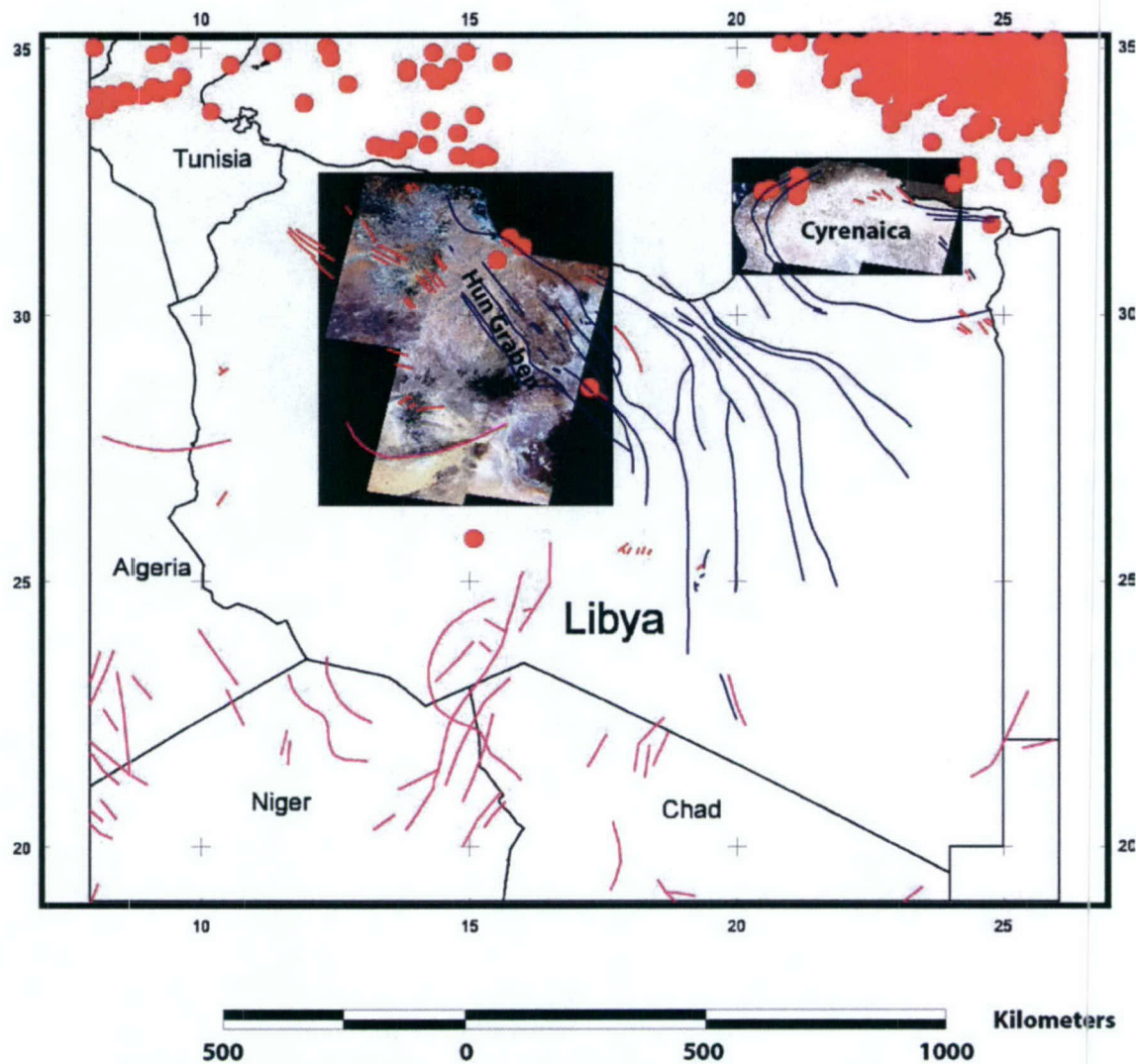


Figure 6. This figure shows the two mosaicked area overlain by mapped faults in Libya. The blue faults are faults that cut Precambrian and younger rocks (Goudarzi et al., 1978), the red faults cut only Mesozoic (Goudarzi et al., 1978) and younger rocks, and the magenta faults are other mapped faults of unknown age in the region (Hearn et al., 2001). The red dots show the seismicity of the region (1975-2004). Earthquakes are of magnitude 3.5 and above (NEIC PDE catalog) (see Table 1).

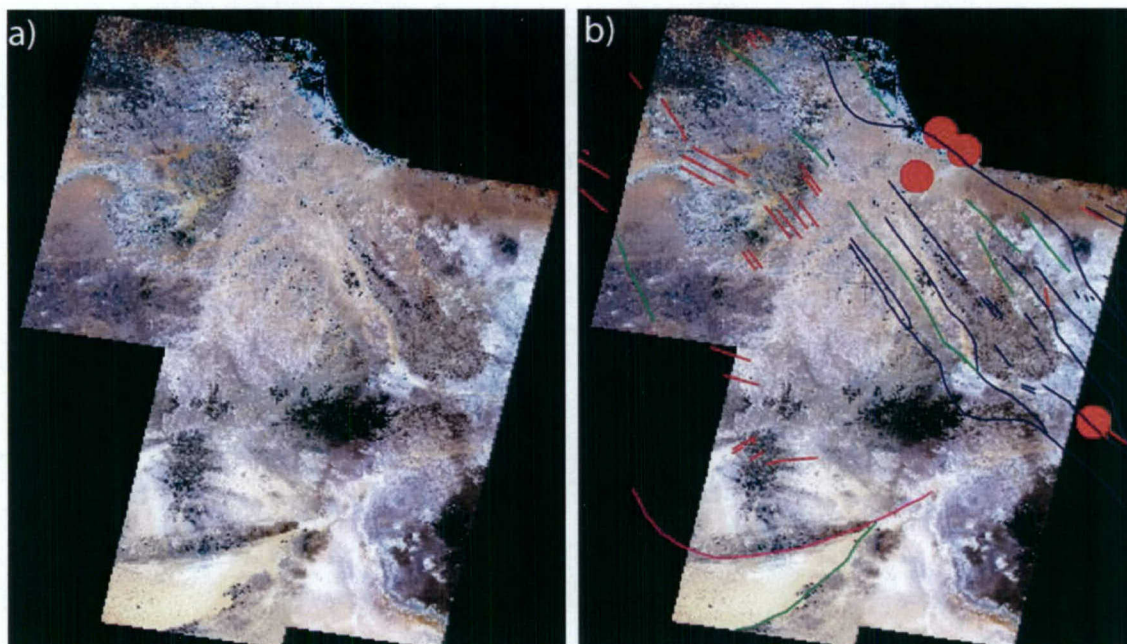


Figure 7. This figure shows the nine mosaicked images for northwestern Libya. Part a) shows the image after mosaicking and part b) shows the image overlain by seismicity, mapped faults and assumed unmapped faults (green lines).

Conclusions

Figure 6 and 7 show both mosaics overlain by mapped faults of known age in Libya along with recent seismicity of the region (Table 1). For the mosaicked section of northeast Libya, it is clear that all seven seismic events occurring in the region are associated with the Precambrian aged faults that outline the borders of the Cyrenaica uplift. Faults cutting rocks of Mesozoic age and younger are less extensive and are therefore less obvious on the mosaicked image. For this reason we may not be able to distinguish faults of Mesozoic age from the mosaicked satellite image. However, on zoomed images with directional filters applied, we were able to identify linear features that align with mapped faults that appear to be surface expressions of other unmapped faults.

The results were similar for the mosaicked image for the northwest region. The sharp change in reflectance in the center of the image demarcates the flanks of the Hun Graben, along with the dominantly northwest southeast trending Precambrian faults in the region. Focal mechanism studies by Suleiman et al. (1995) suggest there are high angle faults in this region. Again the faults of Mesozoic age and younger were not extensive enough to be used to predict the location of other faults of the same age on a macroscopic scale. The sharp change in reflectance in the southern portion of the image shows the presence of a mapped fault of unknown age. The principle of cross cutting relationships could not be applied to discern the age of this fault as it was quite isolated from other features of known age. The seismicity of the northwest portion of Libya seems to be mostly associated with faults of Precambrian age. Three out of four of the seismic events in the northwestern region are located along a mapped Precambrian fault, suggesting that these may be near vertical faults if they are linked to the earthquakes. The single event that is located to the east of the nearest mapped fault would also suggest that the fault is dipping to the east and they are linked at depth.

Table 1. List of events occurring in the study region (1975 – 2000). Only events between latitude 18N - 33N and Longitude 25E – 10E are listed in this table. (Source NEIC PDE catalogue).

Date(yy mm dd)	Origin Time(sec.)	Lat. (deg.)	Long.(deg.)	Depth (km)	Mag. (mb)
75 01 01	07:03:51.40	32.46	21.21	39	4.2
75 09 26	22:42:21.40	28.65	17.24	33	
78 06 07	07:21:21.50	25.80	15.09	33	4.1
83 10 17	22:39:07.67	31.29	15.99	10	4.4
87 06 28	00:50:17.86	32.82	24.36	24	5.4
87 09 13	23:55:00.01	32.64	24.37	33	4.1
88 01 28	15:48:08.15	32.41	21.15	10	4.8
88 01 28	19:12:17.11	32.24	21.16	10	4.4
90 05 18	18:27:51.27	31.71	24.80	10	4.3
92 07 01	15:13:32.38	31.47	15.76	10	4.3
93 09 09	00:32:40.17	32.37	20.65	33	4.5
96 10 30	10:43:02.17	32.33	20.50	10	4.4
99 02 10	5:51:50.73	32.97	15.11	10	4.5
99 02 11	8:04:15.07	32.98	15.18	10	4.1
99 02 13	12:31:18.74	32.94	15.19	10	3.9
99 02 14	03:39:11.52	32.98	15.37	10	3.8
99 03 31	09:42:16.53	32.99	14.81	33	4.3
99 06 17	10:18:04.63	32.48	24.09	33	4.1
99 11 07	14:43:35.30	32.61	21.18	10	4.1
00 05 21	22:45:36.12	31.05	15.53	10	3.7

Section 3

THE USE OF FREE AIR GRAVITY DATA TO CONSTRUCT A 3D DENSITY MODEL FOR THE REGION OF LIBYA

Summary

We present a new 3D density model for the Libya region that includes the topographic relief and five individual subsurface layers, the deepest being at a mantle depth of 50 km. The model was derived utilizing over 6 000 gravity measurements in conjunction with other geophysical and geological data obtained from oil exploration, published research, and other academic institutions. To develop the density model, we used "SURFGRAV", a newly developed general purpose gravity modeling program. To evaluate the validity of our model, we computed the predicted Free Air gravity anomalies for the study area and compared our results to the observed Free Air gravity anomalies. The gravity modeling showed that our new density model is able to predict large portions of the observed Free Air anomalies, especially in uplifted areas. With the exception of the northwestern and northeastern regions where data are sparse and thinning of the crust would improve the fit the residual Free Air gravity is less than 50 mGals, indicating that a more detailed model is required to produce a better match between observed and calculated gravity values.

Introduction

The tectonic evolution of Libya has yielded a complex crustal structure, which is composed of a series of basins and uplifts that began forming in the Lower Paleozoic (Goudarzi, 1980). Tectonic deformation has continued to the present time, with continued basin subsidence and eruption of lavas associated with the Tibesti Mountains in southern Libya. A considerable amount of oil exploration has been undertaken in the area and numerous studies have been published on the shallow (<10 km depth) geology and geophysics of the region. In addition, over 6 000 gravity measurements are available for the northern Libya region.

To achieve our goal of creating a 3D density model of the study area, we primarily used SURFGRAV, a general purpose gravity modeling program that bases its computations on representing the earth by gridded Digital Elevation Maps (DEMs) with an associated grid with a map of geologic units (Baker, 2001). In this approach, topography and near surface geology, greatly simplified in conventional gravity interpretations, are included in the model to determine detailed structure lying below the surface. Veilleux (1999) first utilized this technique in a study of the shallow subsurface of the Pajarito Plateau region surrounding Los Alamos, New Mexico, which is an area of extreme topography consisting of surficial and near surface low density volcanic tuffs. Using this technique, Veilleux (1999) was able to better delineate the eastern and western boundaries of the Velarde graben located beneath the Pajarito Plateau.

In this study, we use available gravity data, in conjunction with other geologic and geophysical control, to construct a 3D model of density/geology for northern Libya and surrounding regions. We then applied a DC shift to our calculated Free Air results in order to obtain a range of gravity values that were comparable to the range in observed gravity. We then

compared our resulting calculated gravity values to determine the regions where our density model appears to match the observations.

Geology

Libya is located on the Mediterranean foreland of the African shield. It is a platformal area containing cratonic basins and classic examples of continental rifts and domal uplifts (Figure 8). Precambrian igneous and metamorphic rocks comprise a small fraction (less than 1%) of the surface of the geology of Libya (Suleiman, 1985). There are basement exposures of mainly granitic igneous rocks and some metamorphic rocks in south central Libya in the Tibesti area of the Nubian uplift (Figure 8 & Figure 9). Vachette (1964) used radiometric dating to show that various granitic rocks in the Nubian uplift were formed 500 to 600 m.y. ago. The Ben Ghnema batholith in the center of the Nubian Uplift, northwest Tibesti is a complex of plutons and is considered to be similar in many ways to the southern California and Sierra Nevada batholiths (Pegram et al., 1976; Ghuma and Rogers, 1978). Ghuma and Rogers (1978) concluded that the Ben Ghema batholith was formed by the subduction of oceanic crust westward under a continental margin located in the Tibesti area during the Pan African orogeny. Precambrian rocks are also found further north associated with the Fezzan and Thiemboka uplifts.

Paleozoic sedimentary rocks are widespread over southern Libya (Figure 9). These are mainly marine shales, siltstones, limestones and continental sandstones. There are no mapped Paleozoic rocks outcropping north of latitude 28N. However, they are reported in the subsurface in many drill holes in the northern basins (Suleiman, 1976; Hammuda, 1980).

The Mesozoic era of the region is characterized by the deposition of hundreds of meters of sediments in shallow and deep troughs along the Mediterranean shore (Goudarzi, 1970). Sandstones, shales, limestones, conglomerates, and various undifferentiated rocks of Mesozoic age can be found throughout Libya.

Rocks of Tertiary age (mainly carbonates) are concentrated in the northern part of the country. Pleistocene and Holocene deposits are also widespread forming the Libyan desert, the dunes areas, the gravel plains and the Mediterranean coastal plains (Goudarzi, 1970). A great majority of the Sirte Basin contains Tertiary and Quaternary deposits (Figure 8).

Tertiary and Quaternary olivine, basalts and phonolites cover a large portion of the central part of the country. Piccoli (1970) reported basalts to have an average age of 40 m.y. However, an average age of 45 m.y. was determined for the southern part of the country.

It is only within the last twenty five years that a coherent picture of the plate tectonic history of Libya has emerged. This is partially due to the fact that two distinctively different aspects of tectonics are involved. In broad terms, the evolution of Gondwana

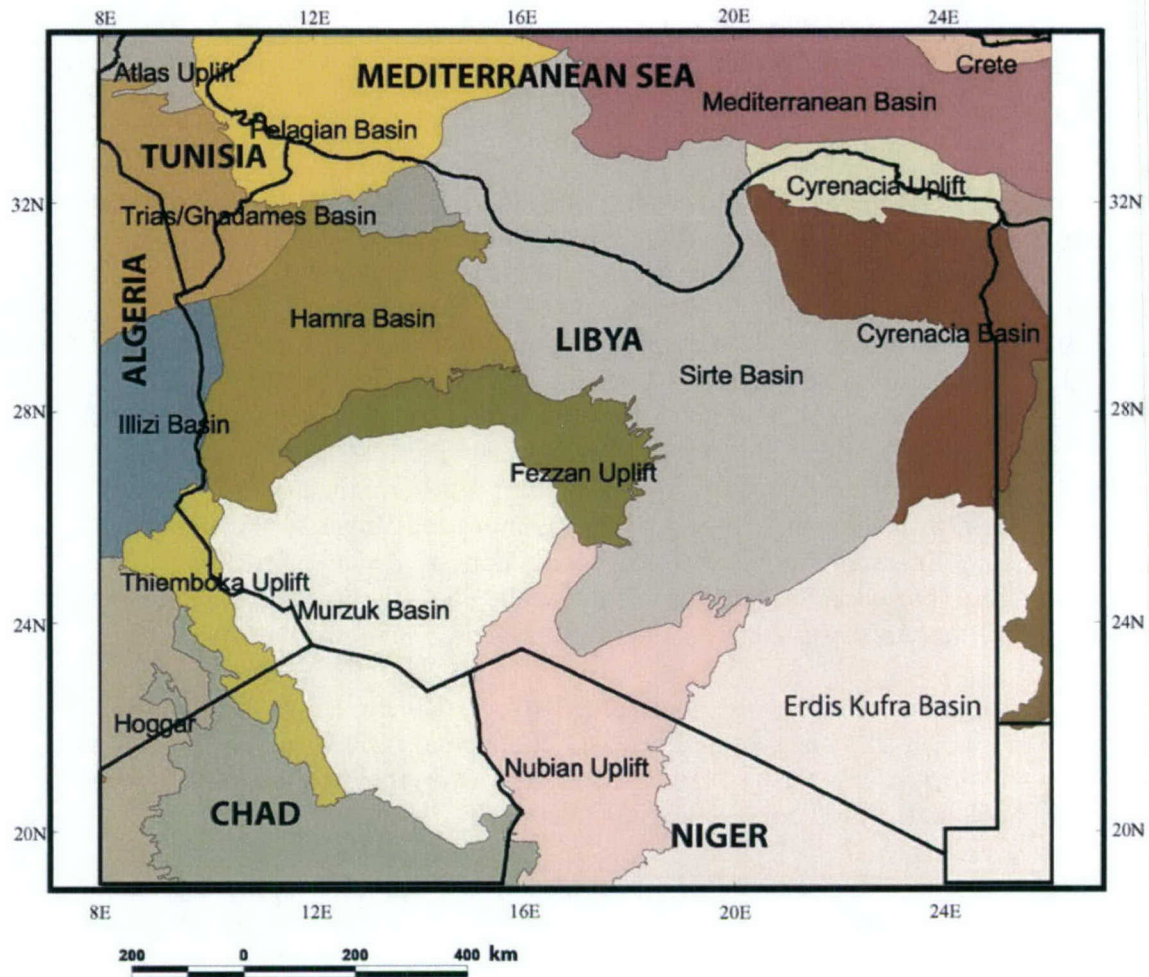


Figure 8. Map of Libya showing the spatial extent of basins and uplifts occurring in Libya (Based on Hearn, 2001).

and Pangaea controlled the development of Libyan tectonics during the Palaeozoic and Early Mesozoic, whereas the evolution of the Tethys and the Mediterranean Seas were the primary controls on the tectonics of Libya during the late Mesozoic and Cenozoic.

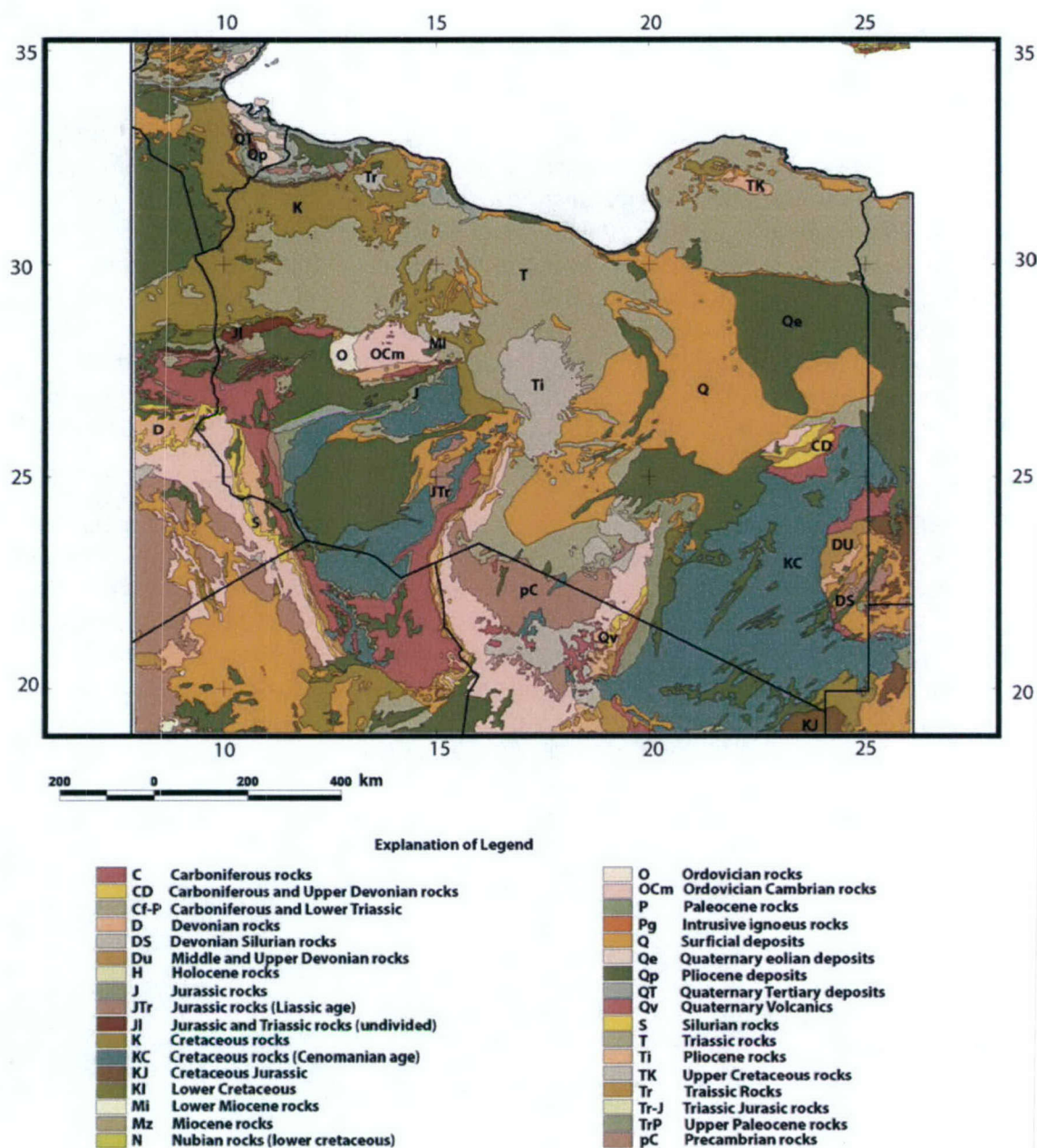


Figure 9. Generalized geologic map of Libya and adjacent areas.

The main evidence for the evolution of the northern margin of Gondwana has come from studies on the ancient cratons and the intracratonic mobile belts exposed in Algeria, Chad, Niger, and Sudan (Hallet, 2002). Given the diverse origins of North Africa, it is not surprising that even after the break-up of Pangaea Africa has not operated as a single plate. The intraplate weaknesses within the African continent have had a significant influence on the tectonic development of Libya (Hallet, 2002).

Previous work

Suleiman et al. (1991) carried out a gravity study of the Sirte Basin in Libya using gravity data archived at the Libyan National Oil Corporation and available from major oil companies. They produced a simple Bouguer gravity map for the Sirte basin which was used for interpretation. They noted an increase in regional gravity values from south to north with a rapid increase at the coastline, typical of the continent-ocean margin due to thinning of the continental crust. They found that the most prominent gravity anomalies correlated well with the structural highs and lows of Libyan basins and uplifts. They also used computer modeling to construct three gravity profiles (one of the profiles traversed the Murzuk Basin, the Fezzan Uplift, the Sirte Basin and the Cyrenaica Basin in Libya) and found that their earth models confirmed the block-faulting nature of the basins and uplifts and indicated thinning of the crust beneath the rifted areas.

Dial (1998) utilized gravity and seismic waveform modeling techniques to determine models of lithospheric structure across northern Africa. He constructed density models using gravity data constrained by previous geological and geophysical studies. He constructed three lithospheric profiles based on Bouguer gravity modeling. One of his three lithospheric profiles traversed Libya (Figure 10 and Figure 11). He also used wavelength filtering techniques to investigate the relative depth and extent of the structures associated with the major anomalies. He noted that the resulting earth model showed slightly greater crustal thickness in the Atlas Mountains (WNW of Libya) than those of previous studies if a low density mantle region is not included. The results also suggested that most of the northern African mantle is fairly homogenous in density with the exception of regions located beneath the Atlas Mountains and to a limited extent beneath the Hoggar Mountains.

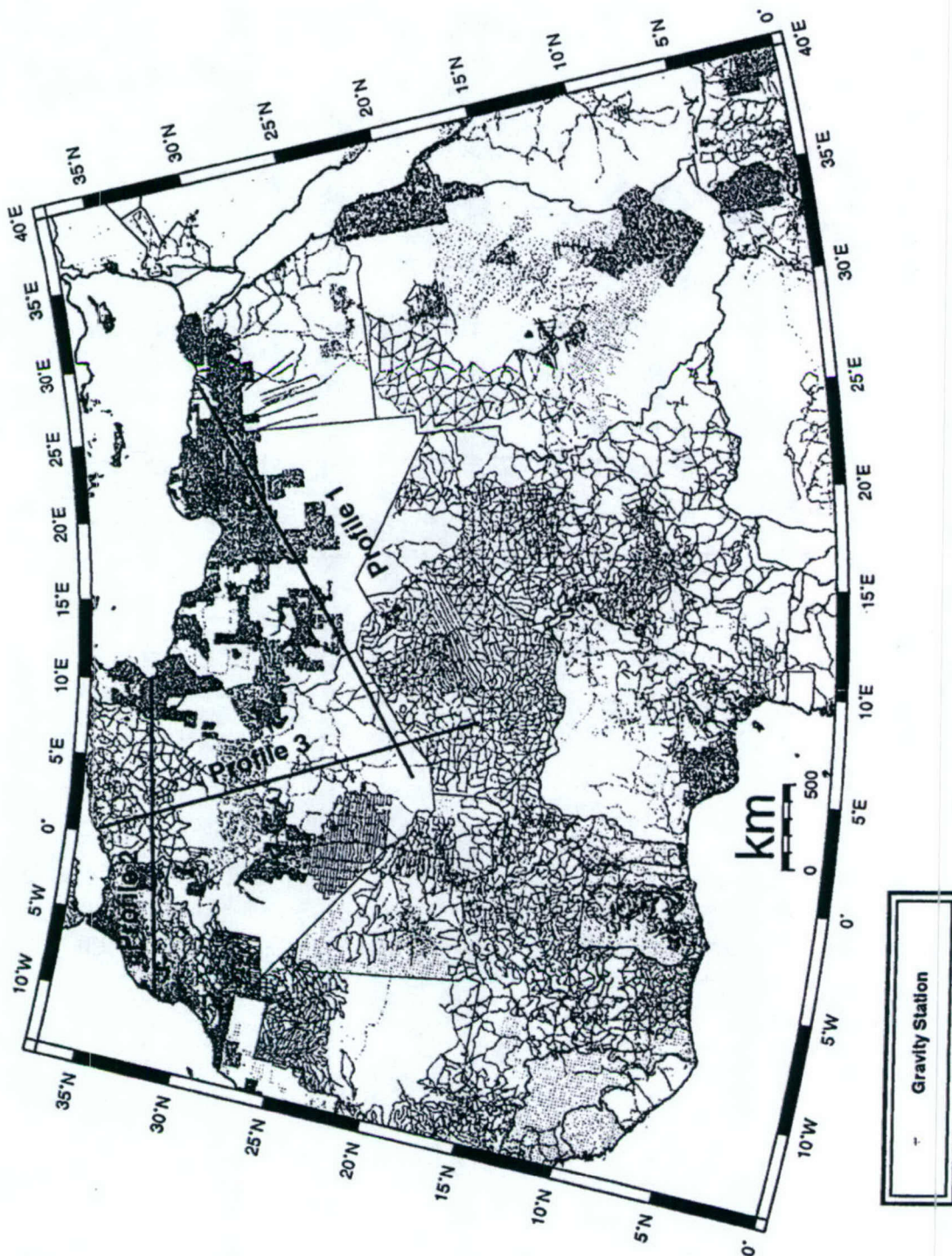


Figure 10. Map of North Africa showing the location of gravity stations and profiles constructed by Dial (1998).

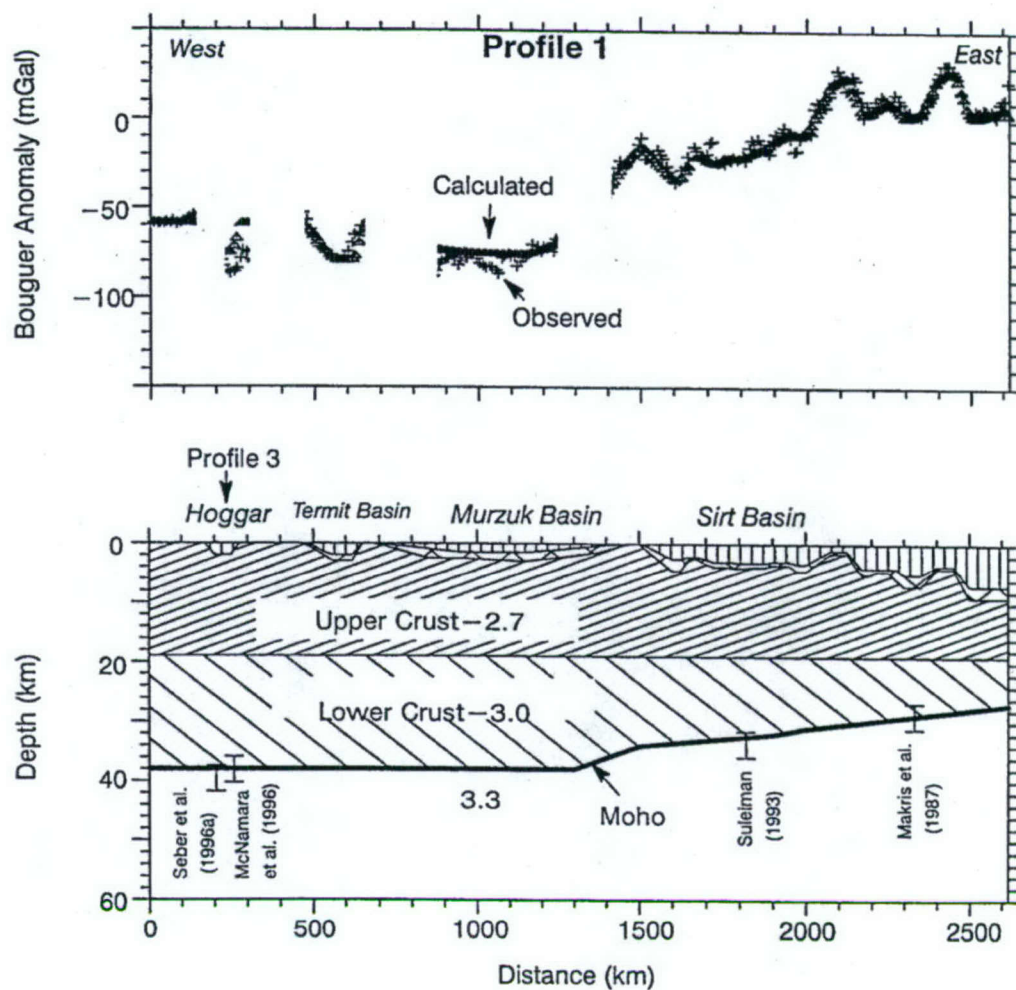


Figure 11. Dial's 1998 model for gravity profile 1 (see Figure 10 for location of profile). The model extends for 2620 km from southern Algeria to northern Egypt (Dial, 1998).

“SURFGRAV”

Carrying out gravimetric terrain corrections is an important and tedious data processing step for work in rugged topography. To deal with this problem the classical method of employing fan-shaped prisms was developed by Hayford and Bowie (1912) and improved by Hammer (1939). Bott (1959), Kane (1962), Nagy (1966), and Plouf (1966, 1977) further developed computer-oriented terrain correction algorithms which represent topography as rectangular prisms. The common “draw-back” related to these methods was that they obtained gravity terrain-correction values by computing volume integrals in which fan shaped or rectangular prisms are used to approximate the topographic relief discontinuously (Zhou et al, 1990). Zhou et al (1990) approximated the land surface using dipping triangular elements, as opposed to the conventional use of prisms, and they found that this triangular element method is more efficient, accurate, and flexible than methods used in previous studies.

The 3D gravity modeling used in this study (SURFGRAV) is based on representing the Earth’s surface by gridded Digital Elevation Maps with associated grids representing tops and bottoms of geologic units (Baker, 2001). The program requires three inputs to be used in the modeling process (Figure 12). They are: a gravity data file, gridded surficial and/or subsurface geology, and a digital elevation model (DEM). The output of the program is the computed gravity due to the model constructed, which is presented as a matrix or spreadsheet data set with each row representing a gravity station, and the columns containing unit-density gravity contributions for each of the geologic units in the area of computation.

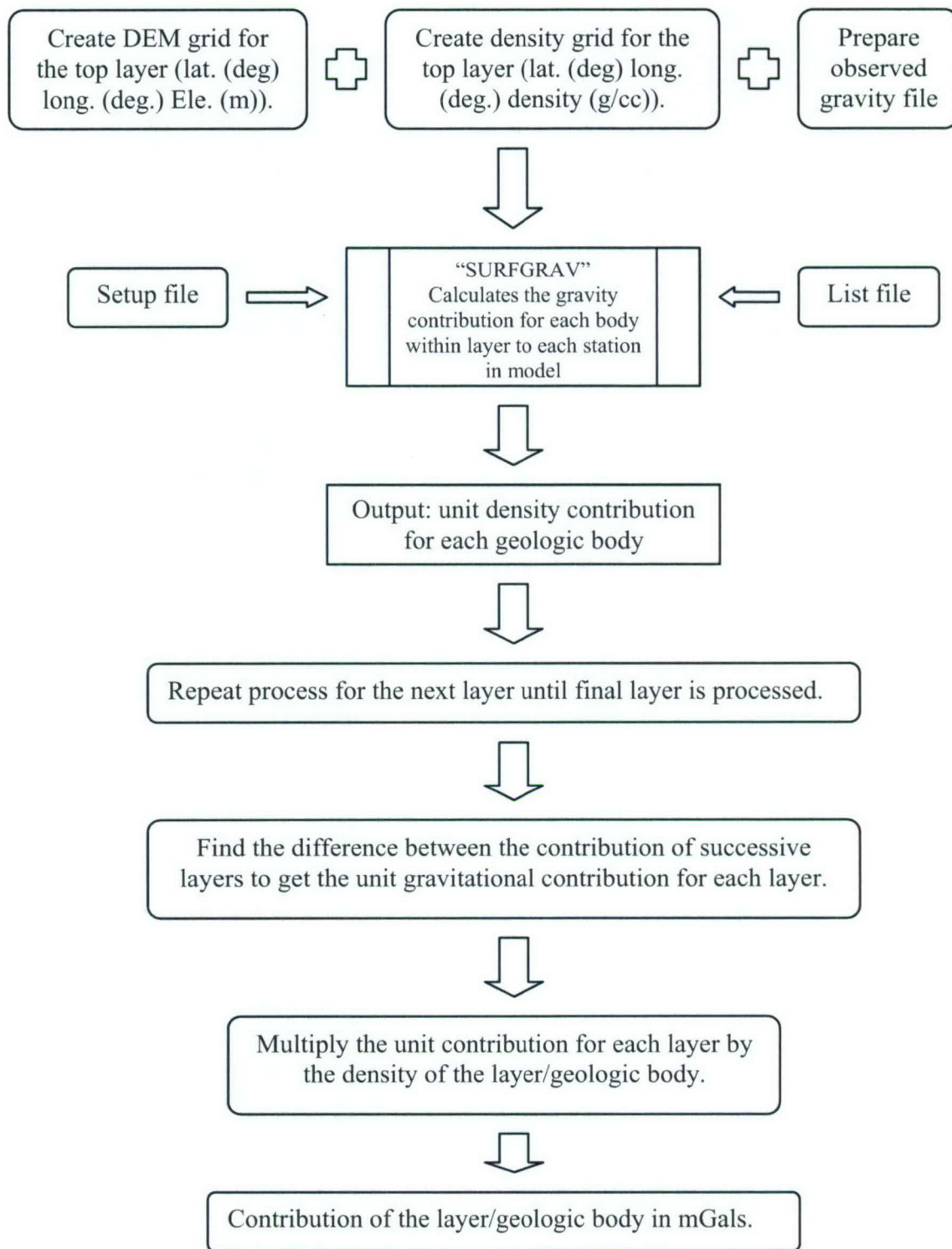


Figure 12. Flow chart for processing and modeling 3D gravity.

Computation Techniques Used in SURFGRAV

Existing topographic DEMs are a poor representation for terrain corrections, as the grid spacing is far too coarse for near station corrections, and far too fine for far station corrections. To speed the process up to the point where the computation can be made with a reasonable effort and accuracy in extreme areas of topography, a number of geologic body representations and numerical approximations are used by SURFGRAV.

First, the typical geologic body is broken into upper and lower surfaces. This makes vertical sided prisms easy to set up and compute. Second the stations are grouped in arbitrary bins and the distance from the bin to the DEM/Geology element determines the calculation technique used by the algorithm (Baker 2001).

The first approximation permits a geologic classification to be associated with the surface of the geologic body. The gravity computation for the upper surface of the geologic body proceeds by accumulating the grid defined prism contributions into their respective geologic classes at a unit density value. The presumed prism extends to infinity with depth. The lower surface contribution can be accumulated in a similar way. These values can be subtracted from the upper surface kernels, giving a vertical-prism type variable density computation (Baker 2001).

For cases where the size of a prism is small, compared to the distance of the station from the prism, an infinite vertical prism is represented by an infinite vertical line element. Within SURFGRAV, all grid/geology elements lying beyond a specific radius (120 km in our case) are computed using the vertical line element formula. The 120 km radius reflects the fact that it is reasonable to use this approximation for regions lying at a radius that is more than 100 times greater than our grid element size of 0.87 km.

In a SURFGRAV setup file one label specifies a list of radii in kilometers at which various approximations are used. The radius at which one wishes to invoke these approximations strongly depends on the granularity of the geology at the scale of the modeling. In this case, we set the point mass radii at 120 km, the row mass at 100km and the adjusted vertical line source at 1 km. Large blocks of homogeneous geology with high topographic relief require larger radii than small blocks of inhomogeneous geology on a flat surface (Baker 2001).

Gravity Data

Over 6000 reduced gravity data points were compiled and used as locations at which to predict gravity values in the modeling process. These gravity points are ultimately used in this study to construct a 3D density distribution throughout the Libya region. The majority of these points were collected from the worldwide gravity database maintained by the National Imagery and Mapping Agency (NIMA) which is now called the National Geospatial-Intelligence agency (NGA). The other points were taken from the gravity database at the University of Texas at El Paso (UTEP). Even though there is a large amount of gravity data available for Libya, the distribution is quite uneven. Approximately, 85% of the gravity data available for Libya are associated with the Sirte Basin. This is due to the high level of petroleum exploration occurring in this region of Libya. There were no gravity data available for regions of Libya located to the

south of latitude 25N. In his previous study Dial (1998) had obtained additional gravity data supplied by GETECH (associated with Leeds University). These data were available to us, but were gridded and thus no station elevations were available so they could not be used. The distribution of the gravity data used in this study is shown in Figure 13.

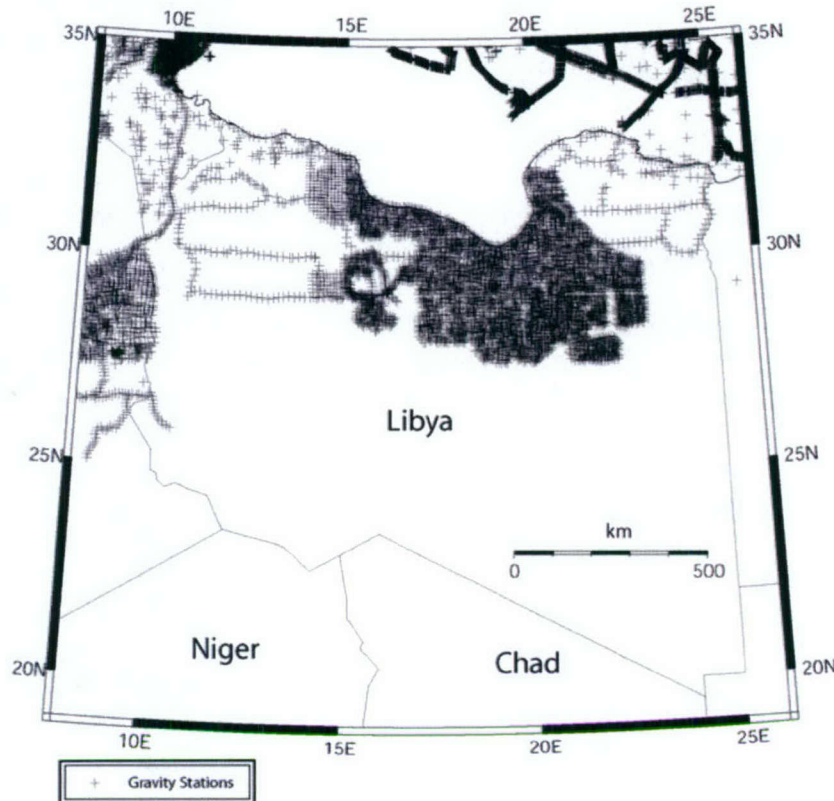


Figure 13. Map of Libya showing the locations of the gravity readings used in this study.

Construction of the Density Model

Topography

The Digital Elevation Model used for the surface of the gravity model was extracted from three main sources: Our UTEP gravity database which had gravity station elevations; GTOPO30, which was released by the USGS (EROS, 1996); and the Global GIS Database: Digital Atlas of Africa, USGS Digital Data Series (DDS62B) (Hearn, 2001). These data sets were merged and gridded at a 30 second interval to form a new combined topography/bathymetry data set. Figure 14 is a 3D grid portrayal of the topography of Libya.

Layers

In an ideal case, each geologic unit of our model would be represented as a separate polygon with an associated density value. If various sediment thicknesses within basins were known or could be calculated, then they would be treated as individual units separate and apart

from neighboring units. However, these distinctions could not be made in Libya, as no data with the appropriate resolution are presently available to carry out this exercise. The Mediterranean Sea was treated as a layer within our model with the thickness estimated from bathymetry. The standard density of sea water, 1.1g/cc, was assigned to this water layer. We proceeded to group the surficial deposits, the Cenozoic, and the Mesozoic units into a single layer, thus assuming a uniform density down to the Mesozoic/Paleozoic interface. The densities assigned to this combined surficial layer were derived by analyzing the geological composition of the outcrops and assigning their average empirical densities based on percentage composition.

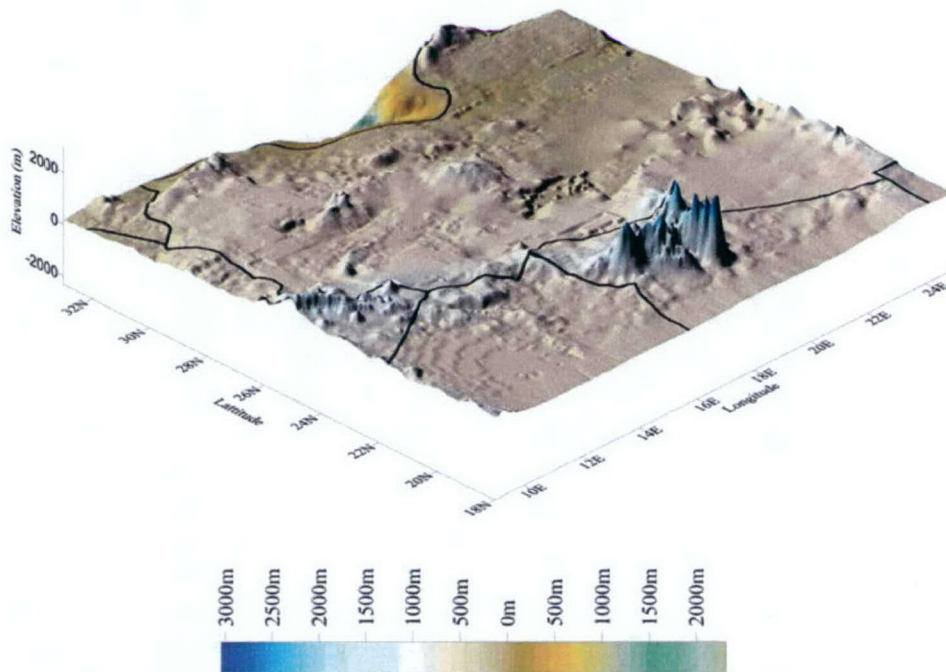


Figure 14. Vertically exaggerated DEM of Libya. The minimum curvature technique was used in the gridding. The gridding was done at 30 sec. spacing. Data used to create the DEM was obtained from the GTOPO30 database. Elevation is in meters.

The empirical densities (Table 2) were obtained from either Carmicheal et al (1989) or Dial (1998). In an effort to reduce the number of geology polygons present in Figure 9, neighboring polygons of geologic bodies having densities within 0.025 g/cc of each other were combined to form a single polygon. Figure 15 shows the resulting average density map of the upper layer of our model.

Table 2. Summarized density assigned to the generalized geology of Libya. Table also shows the age and basic composition of the different units.

Label	Density	Age	Basic Composition
Cam	2.60	Cambrian	course sandstone, quartzitic cement
Car	2.55	Carboniferous	continental sandstone, and siltstone
pC	2.70	Precambrian	quartzite, phyllite, marble, schist, gneiss
Kct	2.45	Upper Cretaceous rocks	limestone, marl, chert, dolomite, shale
Kn	2.50	Lower Cretaceous rocks	Sandstone, conglomerate, claystone
Tmm	2.20	Mid Miocene	detrital limestone, calcareous limestone
Tv	2.72	Tertiary Volcanic	Olivine, basalt, phonolite
Q	2.00	Quaternary deposits	Dunes, loess, alluvium, calcarenite

The base of the Mesozoic and the top of the Precambrian basement were digitized from a 1: 2 000 000 structure contour map of the Libyan Arab Republic and adjacent areas (Goudarzi and Smith, 1978). Both sets of contours were drawn at intervals of 250 m. In northwestern and northeastern Libya north of latitude 30N, marine Jurassic and Triassic rocks are present and serve as reliable controls for the mapping of the base of Mesozoic rocks. Precambrian rocks outcrop in southern and central Libya, again serving as control for mapping the top of the Precambrian basement. The base of the Mesozoic layer and the top of the Precambrian basement defined the boundaries of the Paleozoic layer. The Paleozoic layer was assigned a uniform density of 2.55g/cc. The upper boundary of the lower crust was set at a depth of 19 km, which is consistent with the results of previous studies (Dial, 1998). The density of the Precambrian layer was set at 2.7g/cc as the results of previous gravity models dictated. The density assigned to the lower crust is 3.0g/cc and its upper boundary was set at 35 km depth and its lower boundary was defined by the digitized surface of the Moho (Dial, 1998) (Table 3 and Figure 16).

Yousef (1986) had previously derived a crustal thickness map for northern Africa from surface wave dispersion studies across Africa. The shear velocity model computed for a path across North Africa Platform and the Atlas Mountain suggests an average crustal thickness of 37 km (Yousef, 1986). Dial (1998) improved upon this existing crustal thickness map using constraints from other studies, additional petroleum exploration data unavailable to Yousef (1986) and analysis of Bouguer gravity data. The major improvement made by Dial (1998) was to thin the crust to 38 km in north central Africa near the Tibesti uplift. For the purposes of this study we used a density of 3.3g/cc (Dial, 1998) for the upper mantle. The maximum depth of our model was 50 km, a value selected to be greater than the thickest portion of the crust. Finally, we used a 30 second grid spacing to carry out our density modeling.

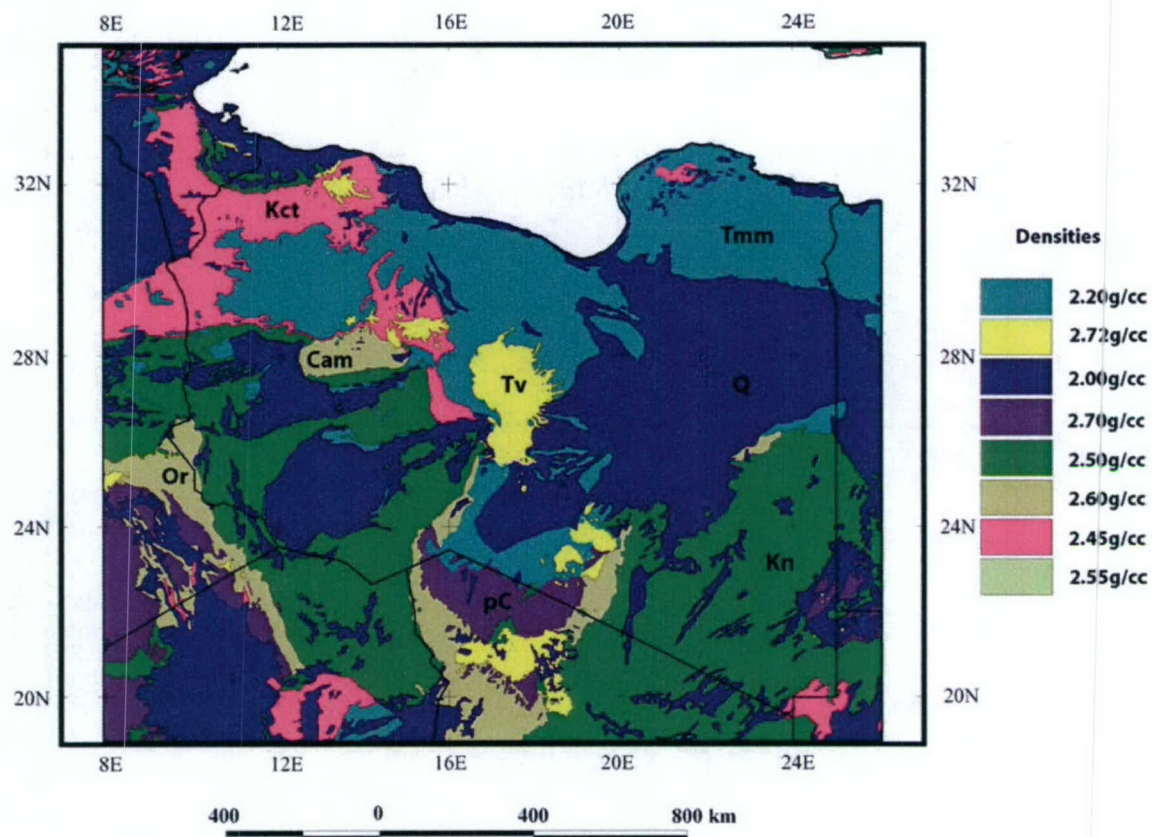


Figure 15. Simplified density map of the surface geology of Libya.

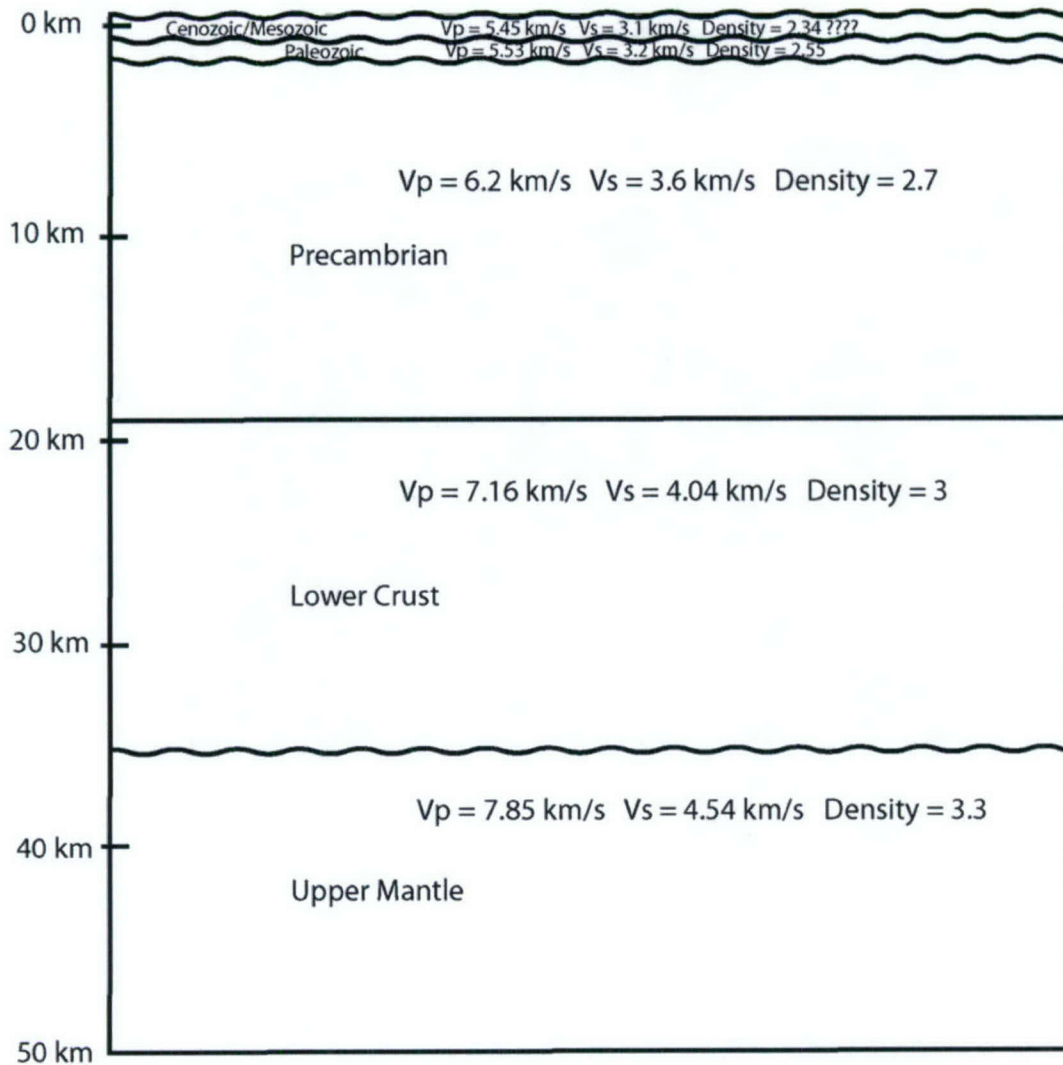


Figure 16. Illustration of the arrangement of the layers used in the density model. The wavy lines represent the irregular surfaces that were obtained from maps and other sources. The upper surface of the lower crust is set at 19 km based on previous studies. The base of the model is at 50 km.

Table 3. Layers used in the density model, along with their average thickness, assigned density and the source from which the densities were obtained.

Layer	Ave Thickness	Density (g/cc)	Source
Mediterranean	0.045 km	1.10	standard
Surficial Layers	1.01 km	2.00 - 2.75	Carmichael (1989)
Paleozoic	1.057 km	2.55	Dial (1998)
Precambrian			
Basement	17.362 km	2.70	Dial (1998)
Lower Crust	15.362 km	3.00	Dial (1998)
Mantle	15.957 km	3.30	Dial (1998)

Results/Discussion

Isopach maps provide a convenient means by which we can visually check the results of the gravitational contribution from each layer. The isopach map of the uppermost layer is shown in Figure 17. The surface layer is thicker in basins and thinner in uplifts, thus we expect the gravitational contribution to be greater in regions with thicker layers. Figure 18 shows the calculated gravitational contribution for the uppermost layer, and we find that in most cases it does resemble the isopach map for the same layer. This indicates that the general lateral density variations in surficial material (Figure 15) were not large enough to overshadow the effect caused by changes in the thickness of this layer. The Sirte basin area generally returned relatively high calculated gravity contributions and so did the Hamra basin. The Cyrenaica uplift returned a lower than average calculated gravity contribution.

Figure 19 shows the result of the summation of the calculated gravity contributions of all the layers to a depth of 50 km. Since the mantle was the thickest and most dense layer used in the study (Table 3) it produced a gravitational contribution that overshadowed the contribution from the overlying layers. In order to meaningfully compare the calculated theoretical gravity with the actual Free Air anomaly, we applied a DC shift to the calculated gravity contributions. The shift was selected to make the range of maximum and minimum values in theoretical gravity comparable to the range of observed data. This enables us to subtract the observed Free Air grid from the resulting calculated Free Air grid to obtain the residual Free Air gravity anomaly. The resulting anomaly map indicates where geologic interpretations may have been misestimated.

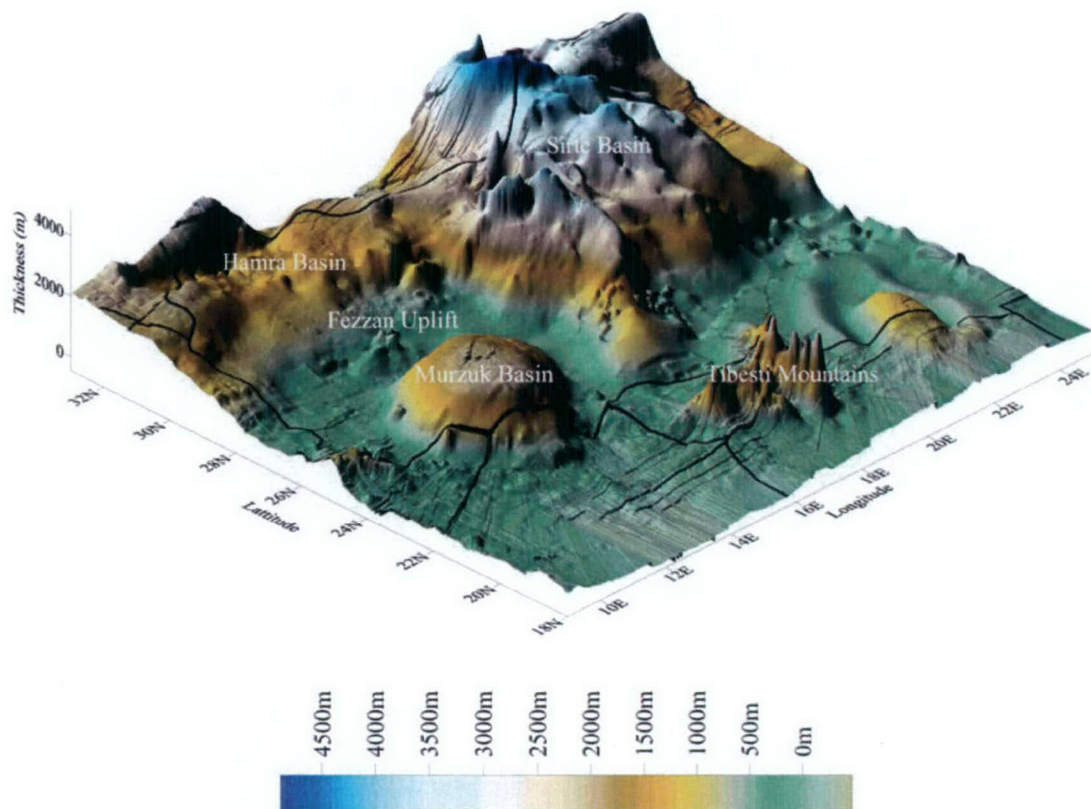


Figure 17. Isopach map of the upper layer of the model. This layer combines the Cenozoic and Mesozoic layers. Basins appear as domes since the layer is thicker in areas where the basins are filled.

In the areas of mismatch the density of bodies may need to be altered or the thickness of bodies adjusted. For example, in areas where there are positive residuals it implies that the density value assigned to a geologic unit was overestimated or the thickness of the unit was overestimated; conversely negative residuals imply underestimation of the density of the geologic unit or the unit thickness.

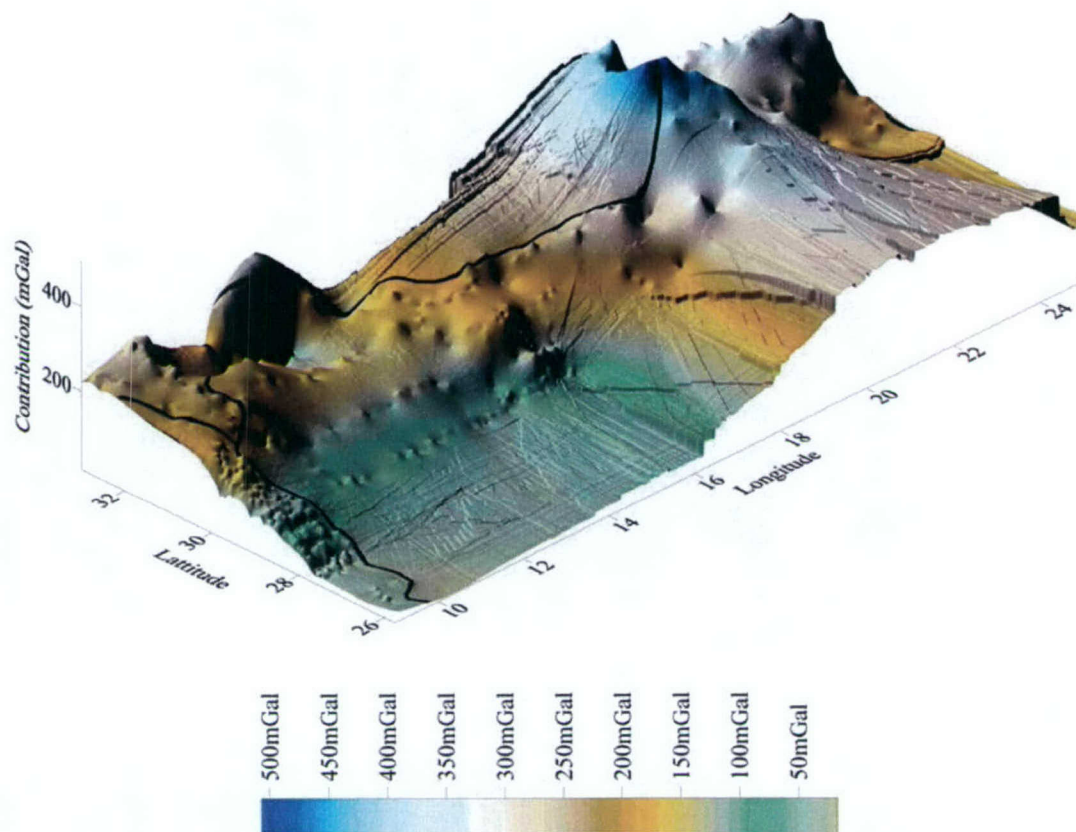


Figure 18. Calculated gravitational contribution of the uppermost layer of the model. Data are unavailable south of latitude 26N, hence the grid is truncated. Note the similarities in where the highs and lows occur as compared with those of the isopach map (Figure 17).

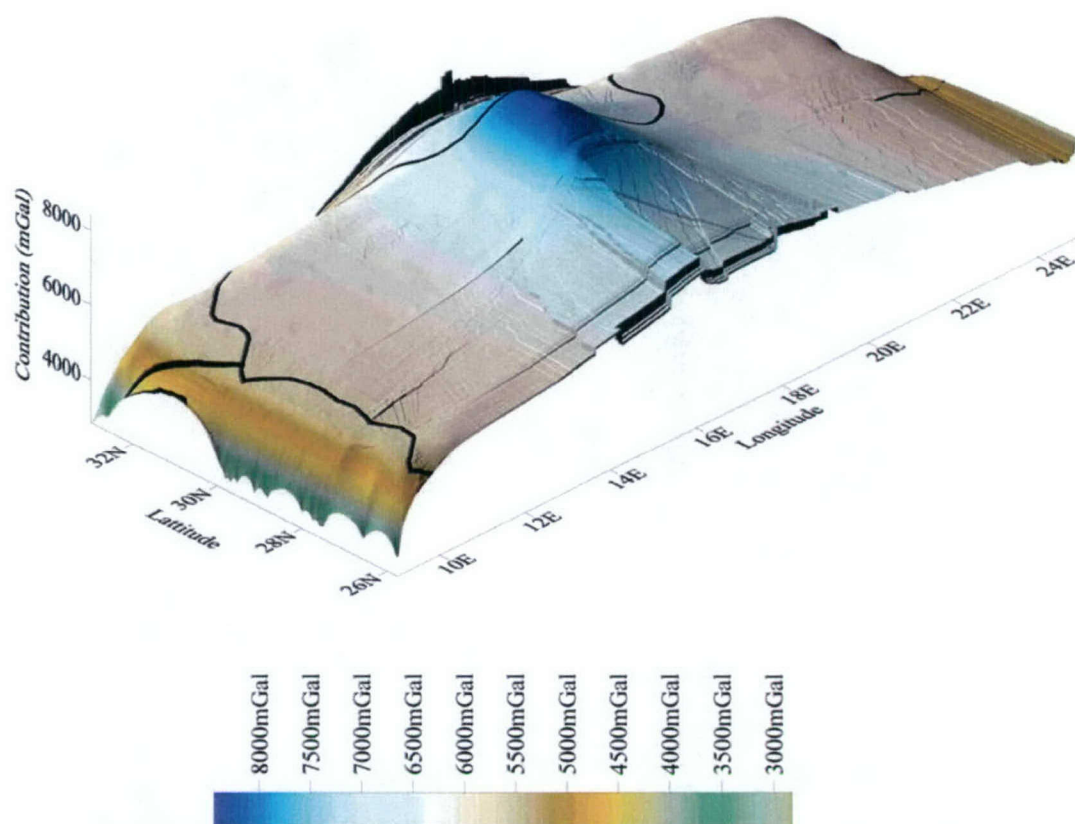


Figure 19. Sum of the gravitational contribution of the layers used in the model. The contribution from the mantle had the most significant impact on the results, as it is the thickest and most dense layer.

The residual Free Air gravity map is shown in Figure 20. The maximum residual was 296 mGal and the minimum was -150 mGal, with 75% of the residual values occurring between 0 to 136 mGal. It is noteworthy that the area with the highest density of data (the Sirte Basin area) is not necessarily the area where we had Free Air residuals closest to 0 mGals. In fact, some of the largest positive residuals occurred in the Sirte Basin. This could be attributed to the fact we assigned a single density to the entire Sirte Basin region down to the top of the Paleozoic layer. The basin fill may not be as consolidated as we estimated which would lead to us overestimating the gravity values. Also our modeling may not have adequately portrayed changes in the thickness of the basin fill, especially for the upper, less dense portions of the basin. We may have also overestimated the theoretical gravity values in the Hun Graben and the Hamra Basin for the same reason. The areas that returned the more suitable density correlation seemed to be those areas that were uplifted, (e.g. Fezzan Uplift and the Cyrenaica Uplift), possibly due to the fact that the density of uplifted areas are more uniform at shallow depth.

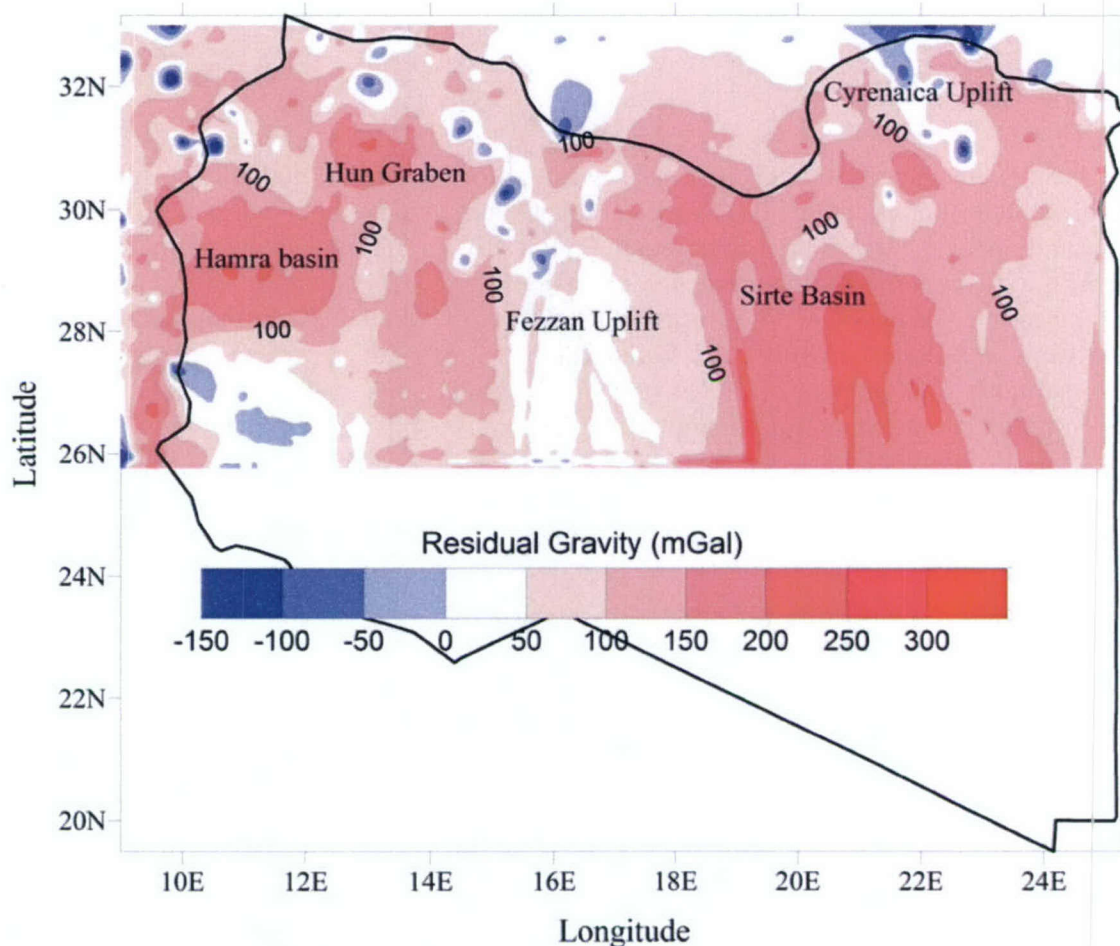


Figure 20. Map showing the residual Free Air gravity distribution. The residual gravity values were calculated by subtracting the observed Free Air gravity from the calculated Free Air values. Positive residual values represent areas where the Free Air gravity was over estimated.

Conclusions

The results of this study show that “SURFGRAV” is a very efficient and effective tool that can be used to estimate gravitational contributions for geologic bodies. We accurately predicted Free Air gravity anomalies for the uplifted regions in Libya, while we generally misestimated anomalies in the basins in the neighborhood of 150 mGals. This suggests that for the basins in Libya, we need additional data to better constrain our model. With more data we would be able to build a more accurate density model and thickness. It is still possible to further refine our model, but at present it is the best density model of crustal Libya available, and it will serve as a framework for deriving a 3D velocity model for Libya.

Section 4

DEVELOPMENT AND VALIDATION OF A 3D VELOCITY MODEL FOR THE LIBYA REGION

Summary

A detailed velocity model for the Libya region will play a vital role in the location of earthquakes and other events within Libya. In this study, we developed a 3D velocity model for the crust and upper mantle in the Libya region (called LIBYA3D) and evaluated its suitability for use as an initial model in tomographic studies. The 3D velocity model of Libya was developed by integrating the results of previous crustal geophysical studies related to crustal studies in the area with the Nafe-Drake relationship. We selected two seismic events occurring in the region that had suitable source receiver paths across the study area and performed 1D and 1.5D validation tests. The 3D model is accurate to within 1.8 seconds in predicting the P-wave arrival times for the events tested and was also useful in producing regional synthetic waveforms that more closely matched the actual regional data than other velocity models for the region. The results of tests performed on the 3D velocity model prove that LIBYA3D will be a particularly good starting model for future studies in the area, which may include wave propagation, regional discrimination and tomographic studies.

Introduction

Confidence in the ability to monitor small and moderate sized events is crucial for the Comprehensive Nuclear-Test-Ban Treaty (CTBT) (e.g., Gitterman et al., 2003). For this reason, it is important to have a 3D velocity model for the Libya region. Libya, as a whole, is not considered a highly active seismic region (Gutenberg and Richter, 1965; Campbell, 1968). However, a few large earthquakes have occurred causing large scale or total damage (Kebeasy, 1980). Some of these earthquakes were described by Minami (1963) and Campbell (1968). 3D velocity models are usually developed using tomographic methods that require the initial velocity model to be a reasonable approximation of the true earth structure (e.g. Johnson and Vincent, 2002). This requires extensive data and station coverage. We instead derive a 3D velocity model (hereafter referred to as LIBYA3D) from *a priori* geophysical data and the Nafe-Drake (1957) relationship which relates density of geologic bodies to velocity.

LIBYA3D was derived from a previous study conducted by Brown et al. (2004) in which they use gravity data to successfully develop a 3D density model for the Libya region. Their density model consisted of a layer representing the Mediterranean Sea, the Cenozoic and Mesozoic combined, the Paleozoic, the Precambrian, the lower crust and the upper mantle (Figure 21). VanDeMark et al. (2004), used this velocity model in a regional discrimination study, and in this study, we use the Nafe-Drake relationship along with other geophysical studies conducted in the area to convert the 3D density model to a 3D velocity model (see Section 5).

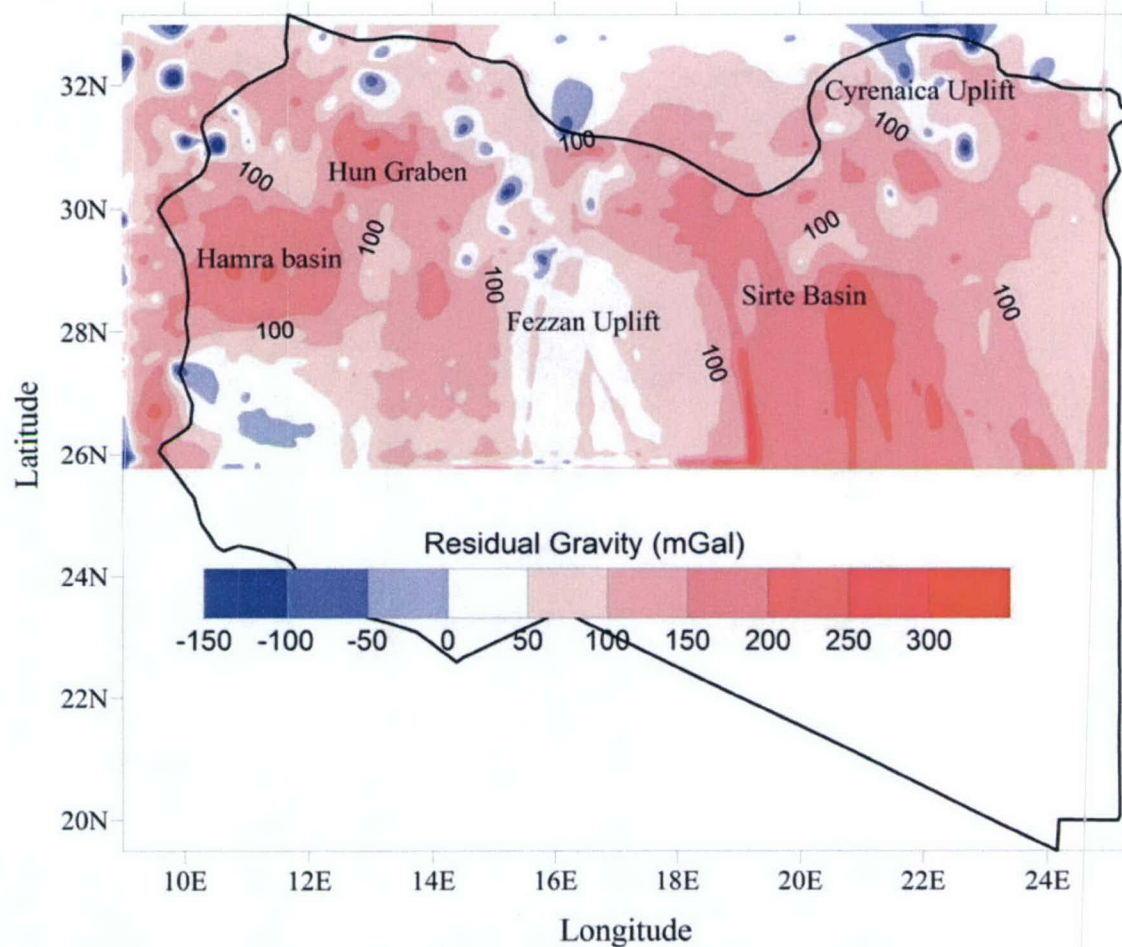


Figure 21. Map showing the residual Free Air gravity distribution. The residual gravity values were calculated by subtracting the observed Free Air gravity from the calculated Free Air values. Positive residual values represent areas where the Free Air gravity was overestimated (from Brown, 2004).

We validated our model by conducting several tests. First, we selected seismic events that were of a large enough magnitude for waveform studies to be performed. The ideal events would preferably be recorded at MEDNET stations and have suitable source receiver paths traversing our area of study. The only two events that satisfied this criteria were event 921012 (ymmdd) ($5.6m_w$) and event 980528 magnitude $5.5m_w$ (Figure 22). In this paper, we present the results of the development and testing of our 3D velocity model (LIBYA3D) using these waveforms. Where possible, we also attempt to compare our results with other proposed velocity models for the region.

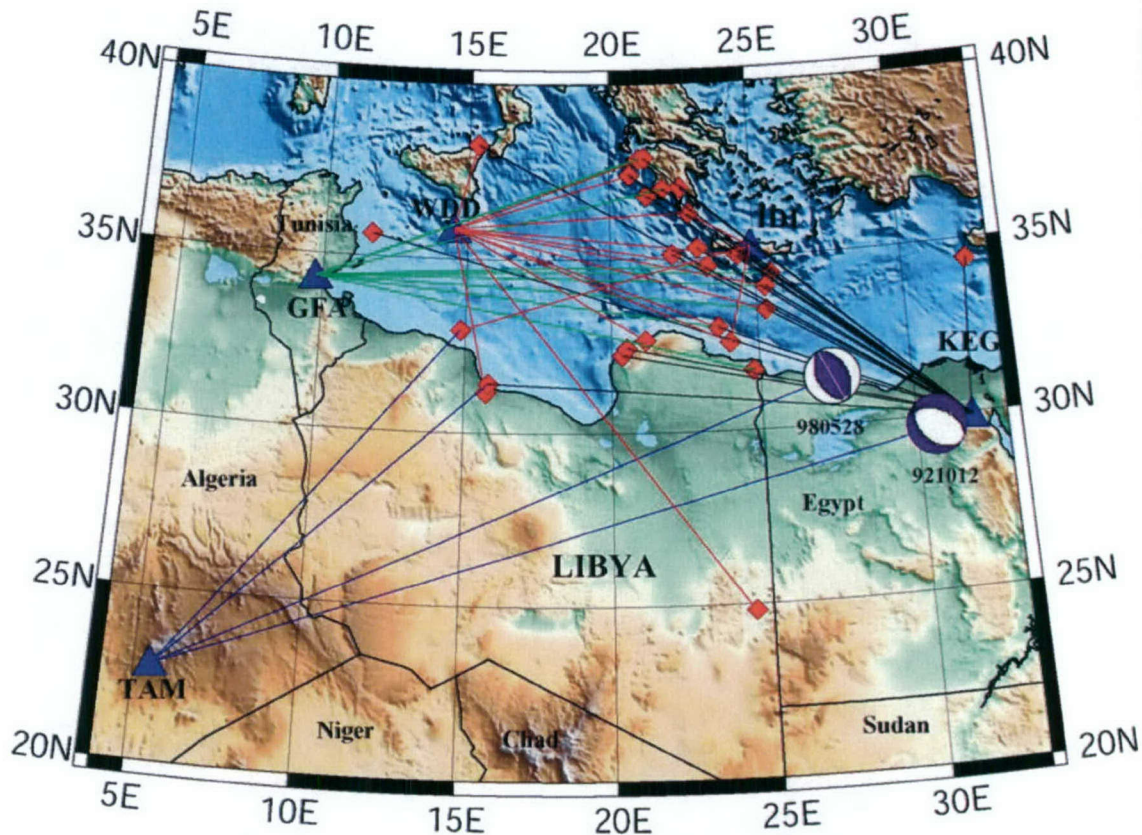


Figure 22. Seismicity map of the Libya region showing earthquakes as red diamonds, stations as blue triangles and the multicolored lines represent source receiver paths. Blue lines show source receiver pathways that were suitable for testing our model. Focal mechanisms indicate the primary events used to validate LIBYA3D.

Existing Geophysical Work

Intense oil exploration activity in Libya during the last 30 years has contributed to the acquisition of extensive knowledge of the geological framework of Libya and its continental shelf. Few regions in the world have such a large amount of geological, geophysical and drilling data available that have been collected in a relatively short period of investigation.

Kebeasy (1980) used data gathered for earthquakes which occurred in and around Libya for the period 262 A.D. to 1977 to investigate the nature of seismicity and seismotectonics of Libya. He also studied the distribution of earthquakes in time and space and calculated the frequency of occurrence of shallow earthquakes in the past 40 years. He found that this distribution of earthquakes in time and space suggests classification of Libya into 3 major seismic zones that agree well with the distribution of major tectonic features. He also found that the damage due to earthquakes covered an abnormally large area around the epicenters and attributed this mainly to the small attenuation of seismic waves generally found in North Africa.

VanDeMark et al. (2004) have utilized LIBYA3D in the context of regional discrimination to investigate small to moderate size natural events (m_b 3.7 – 5.7) in the Libyan region occurring from May 1990 to May 2000. Their observations of P_n and S_n energy at varying frequency ranges (0.5 – 8 Hz) and propagation paths recorded by broadband

instrumentation led them to investigate the attenuation affects of the geologic structure of the Libyan region and the adjacent Mediterranean Sea. Using LIBYA3D, they performed multi-frequency analysis to discern which frequencies have the optimum signal to noise ratio (SNR) for these regional phases. *Pn* and *Sn* showed stronger amplitudes at higher frequencies (4 – 8 Hz) along propagation paths where continental crust is limited. Conversely, they only observed strong *Pn* and *Sn* amplitudes at lower frequencies (0.5 – 4 Hz) along propagation paths where continental crust is prevalent. They further utilized LIBYA3D to study relationships in their data as a function of crustal path and volume. These empirical observations could be used to aid future clandestine explosion discrimination work in the Libyan region if the need arises.

Suleiman and Doser (1995) investigated the seismicity of Libya in order to better understand the earthquake hazards, the tectonics of the region, and the present day evolution of the Sirt Basin. They relocated all the events occurring between 1931 and 1988 (Figure 23), determined focal mechanisms from first motion data, and used waveform modeling to determine the source parameters for the 1935 Mw 7 Hun Graben mainshock and its two largest aftershocks. Their study showed that the Hun Graben is very seismically active. They showed that the majority of the earthquakes of the 1935 sequence occurred along the eastern side of the Hün Graben and seem to align very well in a NW-SE trending fashion along the margin of the graben. The 1939 sequence was found to be located in the Gulf of Sirt. The regions to the NE and NW of the Sirte Basin are seismically active (Figure 23) with almost no seismic activity occurring in the center of the basin itself.

They also used waveform modeling techniques to determine source parameters for the 1935 main shock and its two largest aftershocks. The waveform modeling results suggest strike-slip faulting with a fault plane similar to the strike of the eastern edge of the Hün Graben. The focal mechanism obtained from waveform modeling of the 1935 mainshock differed from that of the first motion studies but was more consistent with the strike of faults within the region. A focal depth of 21 ± 3 km was obtained for this event. More recent activity (1939-1972) appears to have extended NE from the graben into the Mediterranean Sea. Suleiman and Doser (1995) believe that if the zone of active faults associated with the 1935 and 1941 earthquakes extends towards the north-west, it may pose a significant hazard to large cities in the region.

Dial's (1998) modeling of regional and teleseismic waveforms showed that seismic wave propagation throughout the Mediterranean and North African areas is complicated, as would be expected in a zone of plate collision. Dial (1998) made a comparison between the velocity models derived from his study and previous models derived in Africa and the Mediterranean and found that the upper 100 km of all models are very similar. Observations from his waveform modeling led him to conclude that: 1) either a pronounced high-velocity layer lies just below the asthenosphere and/or attenuation of the *Sn* phase exists throughout much of the Mediterranean and northern Africa in order to match observed waveforms or 2) the 1-D reflectivity modeling technique used in his study (Randall et. al., 1995) was insufficient to model the actual complicated 2-D to 3-D structure of the area.

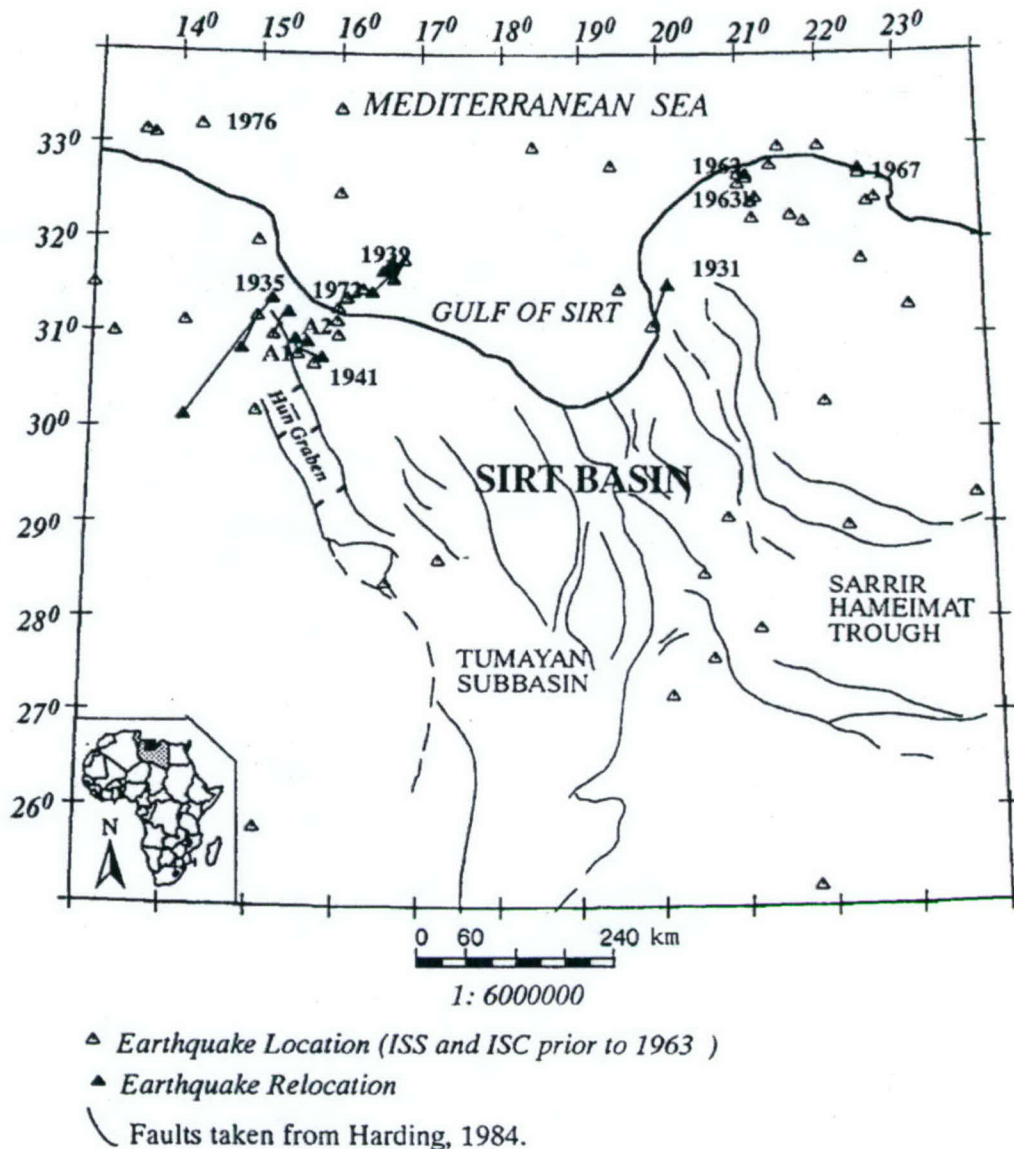


Figure 23. Epicenters of Libyan earthquakes (1931 – 1994). Relocated earthquakes are denoted by solid triangles (from Suleiman and Doser, 1995).

Pasyanos and Walter (2002) attempted to estimate the crust and upper-mantle seismic velocity structure in North Africa, southern Europe, and the Middle East using surface-wave dispersion tomography results from a previous study (Pasyanos et. al., 2001). Their surface wave tomography study provided high-resolution coverage across the region for more than 6800 Rayleigh and Love wave paths over waveform periods from 10-60s. They included additional tomography results from periods of 65 to 120s. The tomography models provided average Rayleigh and Love wave dispersion curves for each 2° x 2° block in the region. They also used the results to determine the velocity structure by fitting the synthetic curves from simplified crust and upper mantle models to the tomographic data for each block via a grid search. Finally, they

compared and contrasted their preferred velocity model with a number of other published models for the region and found that they were similar.

Brown et al. (2004) presented a new 3D density model for the Libya region that included six individual subsurface layers down to a mantle depth of 50 km. Their model was derived by utilizing over 6000 gravity measurements, in conjunction with other geophysical and geological data obtained from oil exploration, published research, and other academic institutions to develop a 3-D density model for the Libya region. They evaluated their model by using it to compute predicted Free Air gravity valued for the region and comparing their results to the observed Free Air gravity anomalies. Their results are shown in Figure 21.

Geophysical Model Development

Our 3D velocity model (LIBYA3D) consists of five individual lithospheric layers. The layers are the uppermost layer (a combination of the Cenozoic and the Mesozoic layers), the Paleozoic layer, the Precambrian layer, the lower crust, and the upper mantle. Data for defining each layer were developed using previous 3D geophysical studies as *a priori* information. We relied heavily on a density model developed by Brown et al (2004) as an initial starting model. The topography of the surface of Libya was extracted from GTOPO30, which was released by the USGS (EROS data collection, 1996). The surficial sediments were combined with other rocks of Cenozoic and Mesozoic age for the first layer of the model since there was no easy way of separating these layers. The Nafe-Drake relationship was used to assign a V_p of 5.45 km/s and a V_s of 3.1 km/s to the uppermost layer (Figure 24 & Figure 25) of our 3D velocity model as derived from density. Our assigned V_p and V_s are comparable to those of previous studies conducted by: Dial (1998) $V_p = 4.75$ km/s, $V_s = 2.6$ km/s; Gumper and Pomeroy (1970) $V_p = 5.8$ km/s, $V_s = 3.4$ km/s; Qiu et al. (1996); $V_p = 5.0$ km/s, $V_s = 2.8$ km/s and Blanco and Spakman (1991) $V_p = 6.2$ km/s. The IASPEI91 (Kennett, and Engdahl, 1991) model is a global model and therefore the V_p and V_s for the shallowest layers were combined and remained undifferentiated. The bottom of LIBYA3D's upper layer was derived from a 1: 2,000,000 structure contour map of the Libyan Arab Republic and adjacent areas (Goudarzi, and Smith, 1978). The contour map was drawn at intervals of 250 m. The average thickness of the combined uppermost layer is approximately 1 km with a maximum thickness of 4.9 km occurring in the Sirte Basin area.

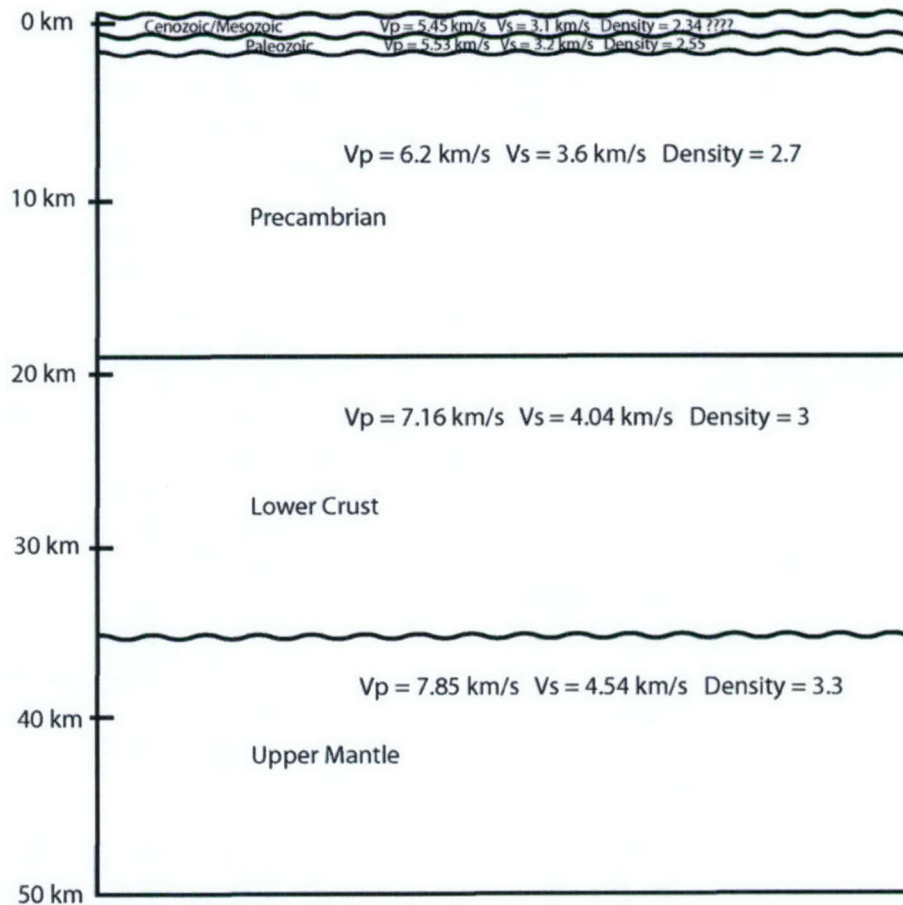


Figure 24. Average 1D velocity model beneath Libya. The wavy lines indicate surfaces that were digitized from data. A uniform depth of 19 km was assumed for the top of the lower crust. Density values are given in g/cc.

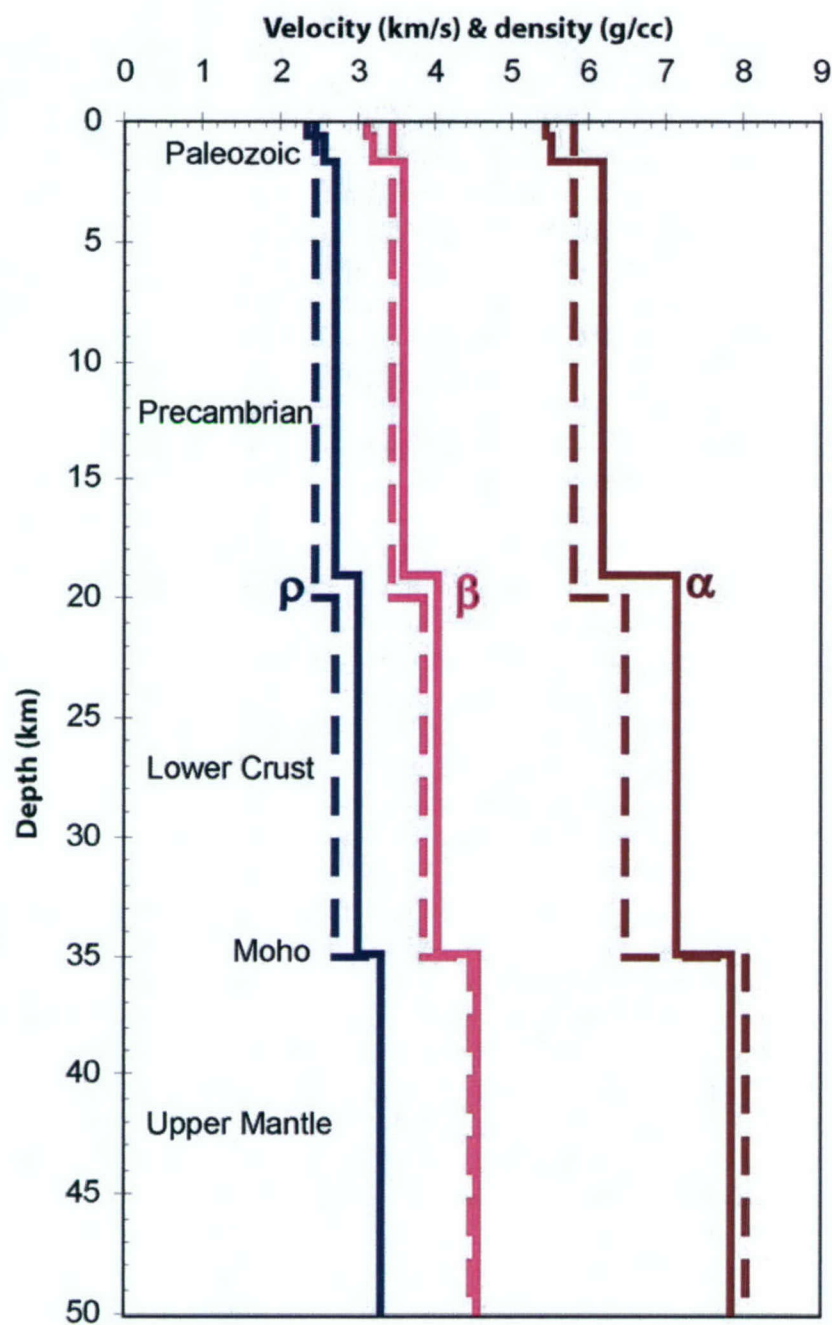


Figure 25. The velocity/density model resulting from our study. Dashed lines represent the IASPEI91 model.

The base of the Mesozoic layer is the top of the Paleozoic layer. Paleozoic sedimentary rocks outcropping in Libya also serve as good control to determine the extent of the Paleozoic layer. We used the Nafe-Drake relationship to assign a V_p of 5.53 km/s and a V_s of 3.2 km/s to

the Paleozoic Layer. These velocities are again comparable to those of previous studies from Dial (1998), Gumper and Pomeroy (1970), Qiu et al. (1996) and Blanko and Spakman (1991). The Paleozoic layer has a maximum thickness of 4.2 km beneath the Hamra basin, northwest Libya. The average thickness of the Paleozoic layer is 1.06 km. The Paleozoic layer is intruded by volcanic igneous rocks in sections of the Fezzan Uplift region, western Libya.

The top of the Precambrian basement rock was also derived from the 1: 2,000,000 structure contour map of the Libya region (Goudarzi, and Smith, 1978) that was drawn at intervals of 250 m. The V_p and V_s for this layer were set at 6.2 km/s and 3.6 km/s, respectively, from the Nafe-Drake relationship. These estimates are reasonable extrapolations of the velocity for rocks of Precambrian age (Dial 1998). The average thickness of the Precambrian layer for the study area beneath Libya is 17.4 km, with a region of maximum thickness exceeding 19 km to the west of the Fezzan Uplift where it outcrops.

Not much information is available for the boundary between the Precambrian basement and the lower crust and for this reason we assumed a flat surface separating these two layers. We used results from previous studies (Dial, 1998) to set this boundary at 19 km and a density of 3 g/cc. For this density V_p and V_s extrapolated from the Nafe-Drake relationship were 7.16 km/s and 4.04 km/s, respectively. The thickness of the lower crust ranged from 20.5 km in southern Libya, thinning to 8.4 km in the north.

The Moho surface reflects the thinning of the crust towards the north of Libya as shown by Dial (1998) and Yousef (1986). The maximum depth chosen for the original density model was 50 km, as it was greater than the thickest region of the crust. V_p and V_s for this portion of the upper mantle were set at 7.85 km/s and 4.54 km/s, respectively (Figure 24 & Figure 25).

P-wave velocities of the LIBYA3D velocity model at depths of 0 km, 1 km, and 3 km are shown in Figure 26. These slices demonstrate lateral velocity variations within the model. Specific features in the velocity model can be correlated with specific geologic or tectonic elements in Libya. For instance, a low velocity region indicating sediment cover in the northern part of the country is clearly visible in Figure 26a and Figure 26b. This low velocity region is due to the presence of the Sirte Basin in the north and north east of the country and the Hamra and Ghadames basin to the northwest of the country (Brown et al. 2004). The oval shaped low velocity zone in the south east part of the country corresponds to the Murzuk basin (Brown et. al, 2004). Two patches of high velocity in Figure 26a correlate with the Fezzan uplift in the north and the Nubian uplift to the south (Brown et al, 2004).

Overall the resulting velocity/density model showed a good correlation with the IASPEI91 model in all three categories (V_p , V_s and density). The values for the P -wave S -wave and velocities from the IASPEI91 model slightly overestimate velocities derived from densities for subsurface Libya. For the Moho both models returned identical values for P - and S -wave velocities; however, a density of 3.3 g/cc was assigned to our model as opposed to 3.396 g/cc in the IASPEI91 model. The widest margin of disparity occurred within the lower crust where the IASPEI 91 P -wave velocity estimate is 6.5 km/s. Other studies (Seber et al 1996, McNamara et al. 1996) also suggest that a higher P -wave velocity exists in North Africa. Dial's study led him to conclude that a value of 7.16 km/s is a more reliable P -wave velocity for the lower crust in this region. The IASPEI91 model shows no differentiation of the layers above the Precambrian Basement.

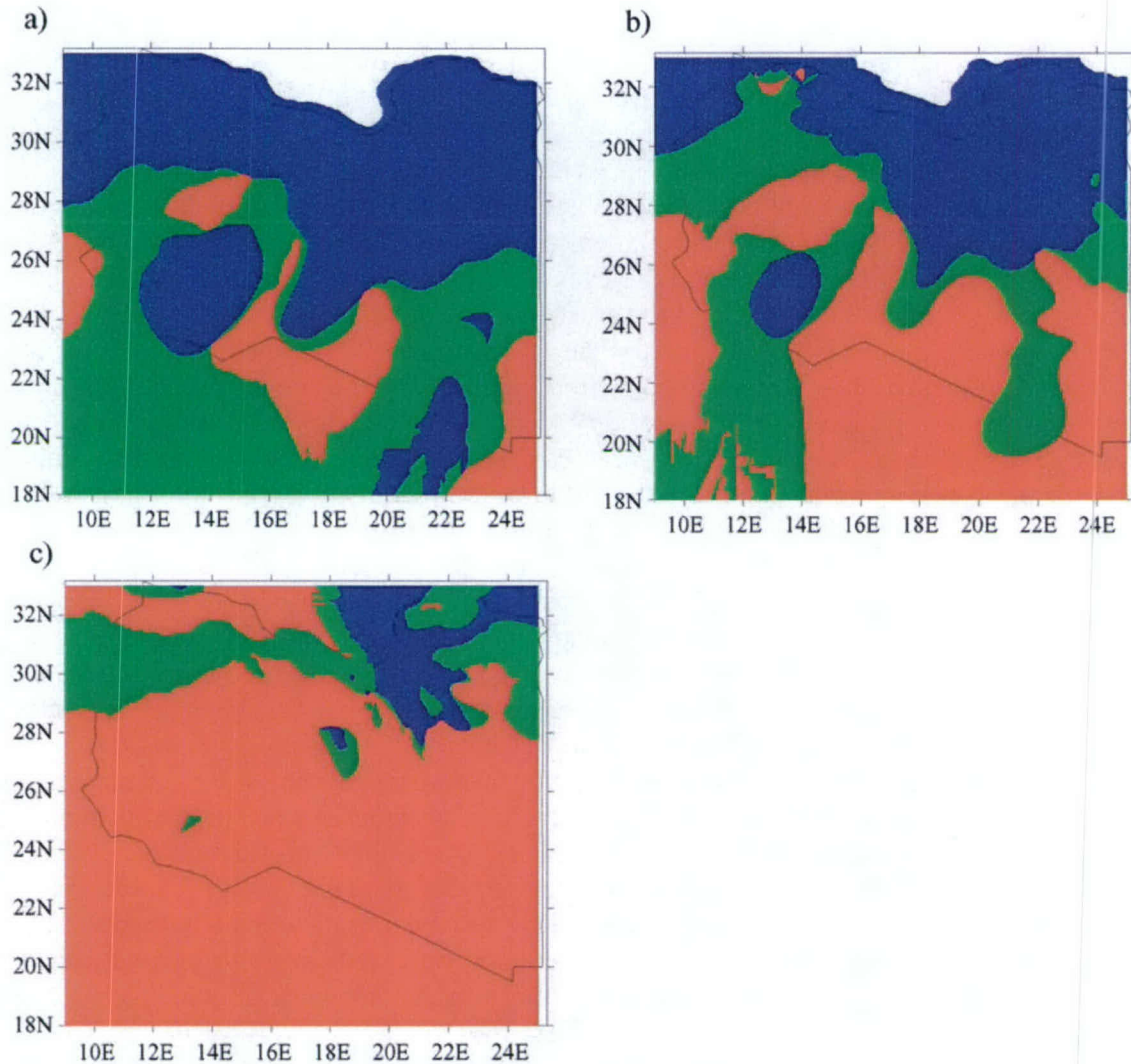


Figure 26. Slices through the LIBYA3D velocity model at (a) 0 km depth, (b) 1 km depth, and (c) 3 km depth. Blue represents areas with a velocity (V_p) of 5.45 km/s and (V_s) of 3.1 km/s. Green represents areas of velocity (V_p) of 5.53 km/s and (V_s) of 3.2 km/s. Red represents areas of velocity (V_p) of 6.2 km/s and (V_s) of 3.6 km/s.

For our LIBYA3D model however, having digitized the surface of the top of the Precambrian basement rock and the base of the Mesozoic surface, we were able to assign boundaries to the uppermost layers of the model. In the Libya region, the crust thins towards the north and so there is significant varying thickness of the Moho. Figure 24 is an average representation of the 1D model so we used the average thickness of the upper mantle which is 35 km, the same as the value used in the IASPEI91 model. In the next section will verify if our velocity model provides significant improvement over IASPEI91 in waveform modeling.

1D Validation of 3D Velocity Model

We carried out preliminary seismic evaluations on the average 1D velocity model using the velocities assigned to the individual layers as shown in Figure 24. For this evaluation we chose events 921012 (YYMMDD) ($5.8m_w$) and event 9980528 ($5.5m_w$) (Figure 22). We obtained locations for these events using a bootstrap technique after Petroy and Weins (1989). These events had large enough magnitudes to allow good propagation of seismic energy across the Libyan lithosphere. Special care had to be taken when choosing source-receiver pathways since the border between the African plate and the Eurasian plate is situated to the north of Libya. In this area there is considerable thinning of the crust. We utilized the TauP Toolkit (after Crotwell, 2000) to compute a predicted travel time for the P-wave and S-wave of the two events at the Tamanrasset (TAM) station, Algeria and compared the results to the actual recorded waveforms. The results are shown in Figure 27. The red line shows the predicted P-wave arrival time (T_0) for the event generated from our model. The predicted arrival times were accurate to within 1.8 seconds for the P-wave arrival times and to within 5 seconds in predicting the S-wave arrival times, proving that our velocity model has validity in the 1D case.

We then calculated individual path specific velocity models for the same two events in order to analyze our 1.5D velocity model. This was done by calculating the average thickness of each layer along a straight path from the event source to TAM and assigning the resulting thickness to that layer. This is different from the average 1D layer thickness, as the model is path specific. The synthetic waveform was calculated based on the reflectivity technique presented by Kennett (1983) as implemented by Randall (1985). We used the Seismic Analysis Code (SAC) (Goldstein, 1999) to carry out the seismic analysis for this portion of the study. The results of the modeling of the two events are shown in Figure 28. The seismograms are filtered using a band pass Butterworth filter of 10-100s as the most significant waveform information is found in this frequency range. For event 921012 we observed a close correlation between the synthetic and the recorded seismogram on the vertical and transverse components, while we did not receive a good fit on the radial component. For event 980528 we again observed favorable correlation on the vertical component but mismatched the radial and transverse components (Figure 28).

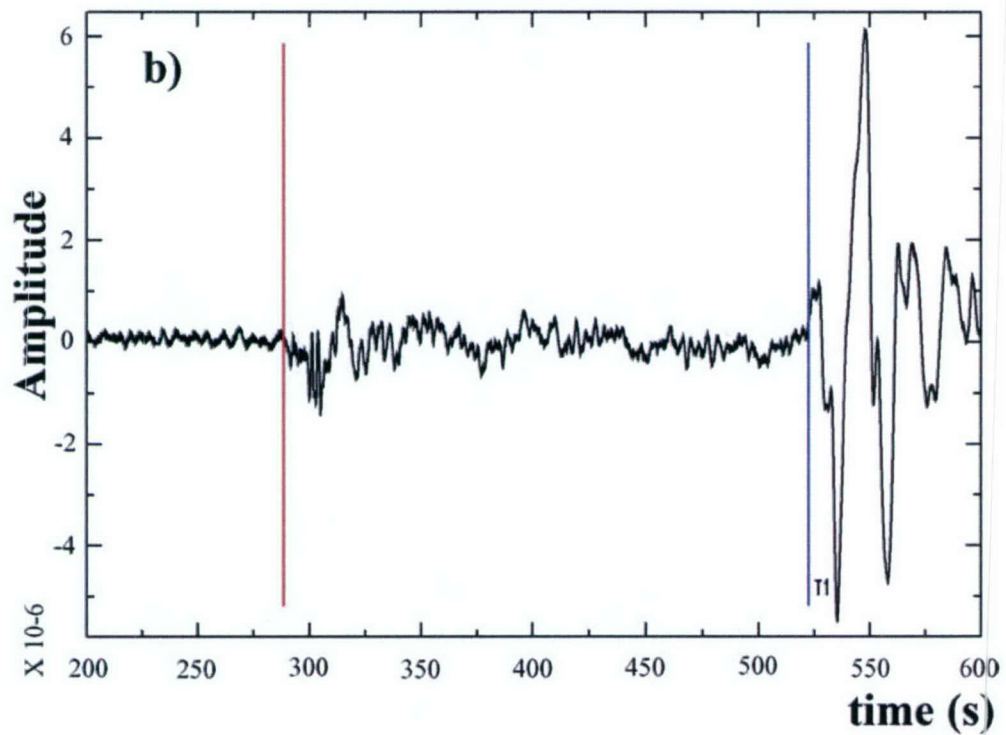
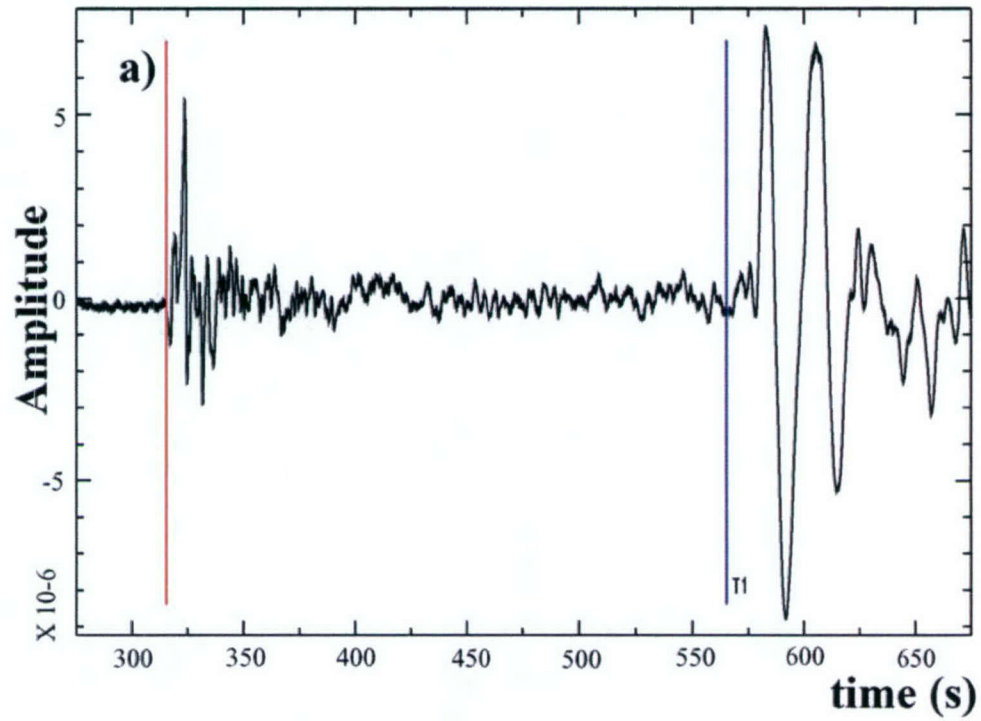


Figure 27. Unfiltered seismogram of a) event 921012 and b) event 980528 recorded at TAM. The arrival time of the P-wave as predicted by our 1D model (red lines) and as well as the predicted S-wave arrival time (blue lines).

Error Analysis

We compared our predicted waveforms to the data by calculating the rms of the mismatches between the observed and predicted waveforms for events 921012 and 980528 recorded at TAM. These events were used as the waveforms had suitably large enough amplitudes to be modeled. The waveforms were calculated as a function of depth to validate the initial depth provided by the Harvard CMT. The initial depths were found to be the most suitable depth for performing the waveform modeling. We then filtered the waveforms at different pass bands and the result of comparisons done at the 10-100s pass band is shown in Figure 29 and Table 1. The comparison was performed over the first 10 seconds of the wave train and Figure 29 shows the resulting error analysis for the three different components of the two sample events using the LIBYA3D, the global IASPEI91 model and the 15 layer model proposed by Dial (1998).

In all cases the LIBYA3D model returned a more accurately predicted waveform for the sampled seismic events than the IASPEI91 model. This was not the case when LIBYA3D was compared to the Dial 15 layer model. Dial's (1998) model was derived from iterative seismic waveform modeling of predicted waveforms compared against earthquake data. This analysis of the waveform data suggests that Dial's (1998) model may have better accounted for surficial layers. However, until we are able to perform 2D and 3D modeling we may not be able to see the true improvement of LIBYA3D as compared to the other models.

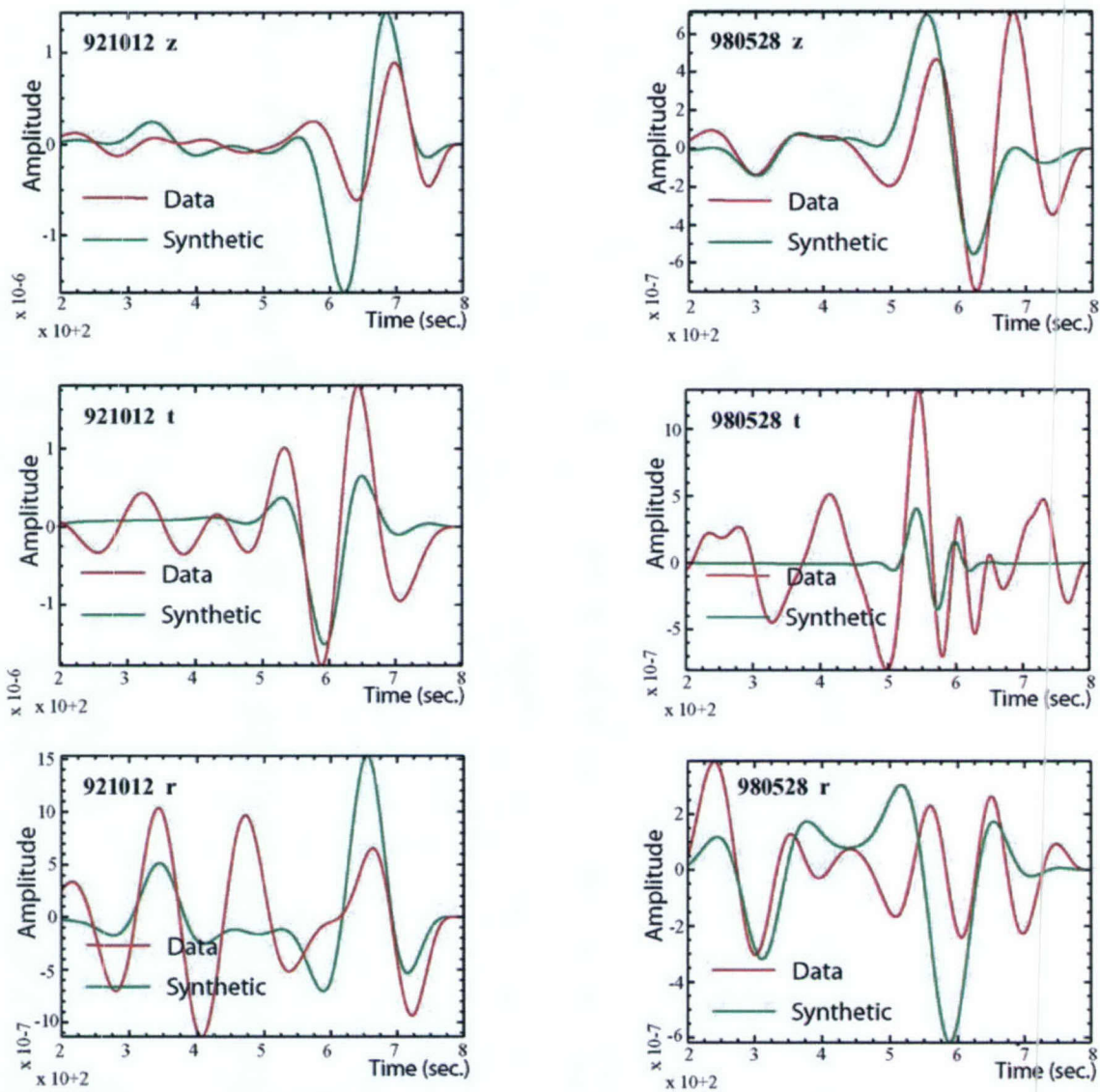


Figure 28. Waveform comparison between synthetic and data for events 921012 and 980528 used in the validation study. The seismograms were recorded at TAM. A band pass (10 – 100s) Butterworth filter has been applied to the data and the synthetic seismograms.

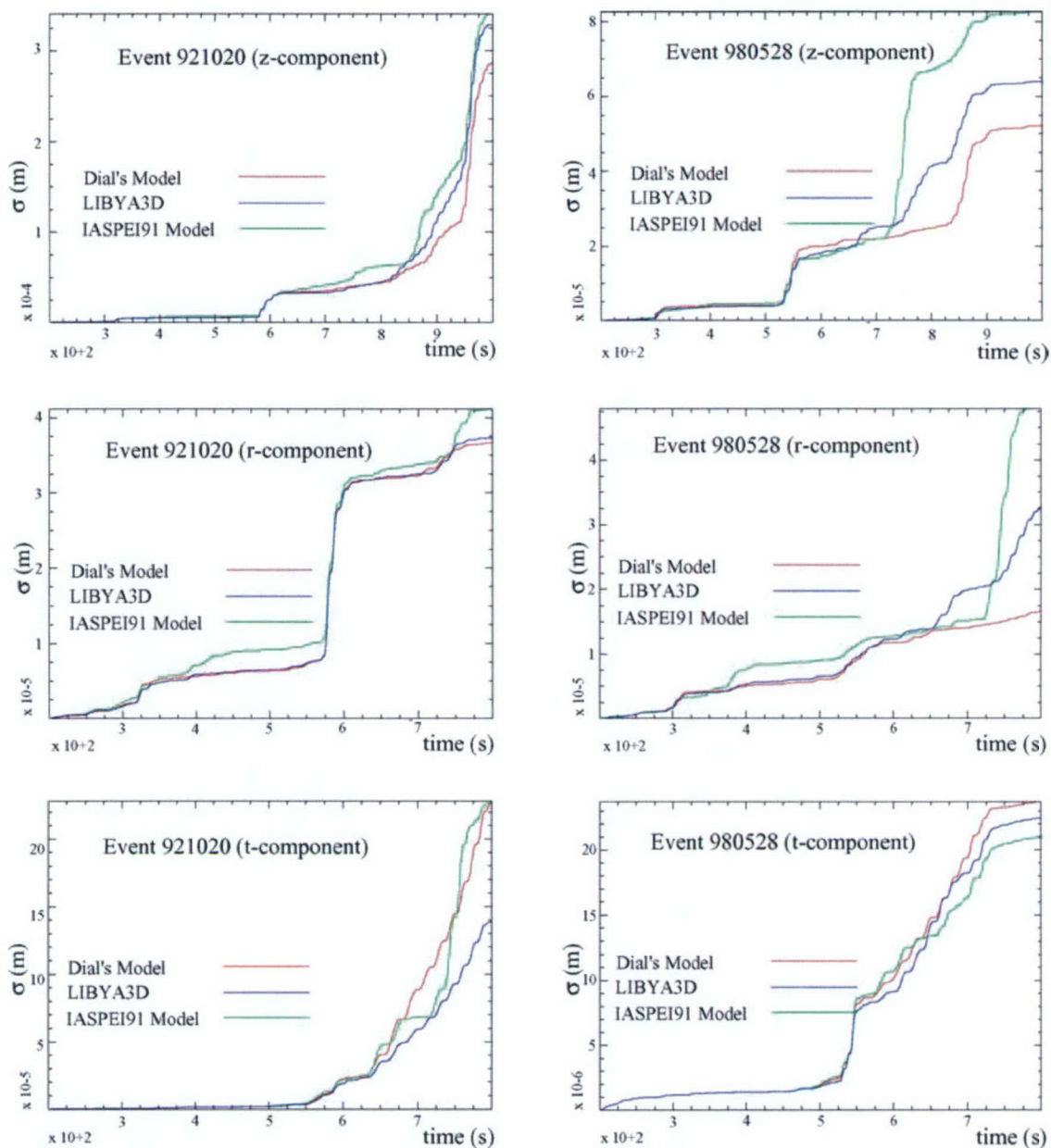


Figure 29. Plots of the results of our 1.5D error analysis exercise. The seismograms were recorded at TAM.

Table 4. Comparison of error analysis results (in amplitudes of meters) of LIBYA3D, IASPEI91 and the Dial Model.

Component	Velocity Model		
921020	libya3D	IASPEI91	Dial (1998)
<i>vertical</i>	6.20E-04	8.25E-04	5.25E-04
<i>radial</i>	3.25E-05	5.55E-05	1.70E-05
<i>transverse</i>	2.25E-06	2.40E-06	2.10E-06
980528	libya3D	IASPEI91	Dial (1998)
<i>vertical</i>	3.45E-04	4.25E-04	2.85E-04
<i>radial</i>	3.26E-05	3.73E-05	3.71E-05
<i>transverse</i>	1.39E-04	2.30E-04	2.30E-04

Conclusions

This paper presents a new 3D velocity model (LIBYA3D) for the Libya region. LIBYA3D was derived from a 3D density model after Brown et al (2004) and is similar in many ways to other previous regional and global velocity models. Tests results obtained by using an average 1D model derived from the 3D structure validated our model as being effective in predicting P- and S-wave arrival times. We were able to further validate our model by producing regional synthetic waveforms that resembled the actual waveforms. In error analysis tests of LIBYA3D using 1.5D approximations to the path returned error values that were comparable to other regional velocity models developed from actual seismic waveform modeling, while outperforming the global IASPEI91 model.

Due to lack of events occurring in the region with suitable source receiver paths, we were unable to thoroughly test our model. However, we remain convinced that our 3D velocity model is unique for the region and it is potentially an excellent starting model for anyone interested in carrying out inversion involving a velocity model for the region. Developing such a 3D model also improves our ability for CTBT monitoring in a complex geologic region such as Libya.

Section 5

ANALYSIS OF HIGH FREQUENCY PROPAGATION IN THE LIBYAN REGION UTILIZING A 3-D GEOPHYSICAL MODEL

Summary

We utilize a 3-D geophysical model, "LIBYA3D," in the context of regional discrimination to investigate small to moderate size natural events (m_b 3.7 – 5.7) in the Libyan region occurring from May 1990 to May 2000. Observations of Pn and Sn energy at varying frequency ranges (0.5 – 8 Hz) and propagation paths recorded by broadband instrumentation led us to investigate the attenuation effects of the geologic structure of the Libyan region and the adjacent Mediterranean Sea. We perform multi-frequency analysis to discern which frequencies have the optimum signal to noise ratio (SNR) for these regional phases. Pn and Sn SNR show stronger amplitudes at higher frequencies (4 – 8 Hz) along propagation paths where continental crust is limited. Conversely, we only observe strong Pn and Sn amplitudes at lower frequencies (0.5 – 4 Hz) along propagation paths where continental crust is prevalent. We utilize LIBYA3D to develop relationships in our data as a function of crustal path, Moho variance, and volume. These empirical observations could be used to aid future clandestine explosion discrimination work in the Libyan region if the need arises.

Introduction

To monitor a zero yield nuclear explosion treaty, we must be able to analyze events of all magnitudes that occur throughout the world. However, it is difficult to analyze the effectiveness of discriminating between earthquakes and explosions when there are a small amount of events to analyze. Compounding problems arise with small magnitude events recorded at regional distances, since path effects can lead to complex regional seismograms causing misclassification of events (e.g., Velasco *et al.*, 2003). Many regions in the world exhibit these attributes of few events and complex regional propagation, forcing new approaches to be developed in order to effectively monitor for underground nuclear tests.

The Libyan region is a stable continental margin and exhibits some of these attributes, where there are few events, and those that occur are generally small in magnitude. We focus on studying the effectiveness of regional discrimination techniques in the Libya region. We utilize seismic events in and around Libya (Figure 30, Table 5), yet there are no explosion data for Libya. We are further limited by the small number of reliable stations at regional distances. Although there are regional networks in place in Egypt (Helwan) and Algeria (Alger-Bouzareah), the data are not readily available to us. To overcome these issues, we utilize a 3-D geophysical model of the Libyan region, known as "LIBYA3D" (Brown *et al.*, 2004), to help improve regional discrimination in the region. We use LIBYA3D to investigate path effects associated with Signal to Noise Ratio (SNR). We also identify path dependent cross spectral ratios (e.g., Walter *et al.*, 1995) which show the elevated SNR frequency ranges at specific stations as solid parameters for future verification work.

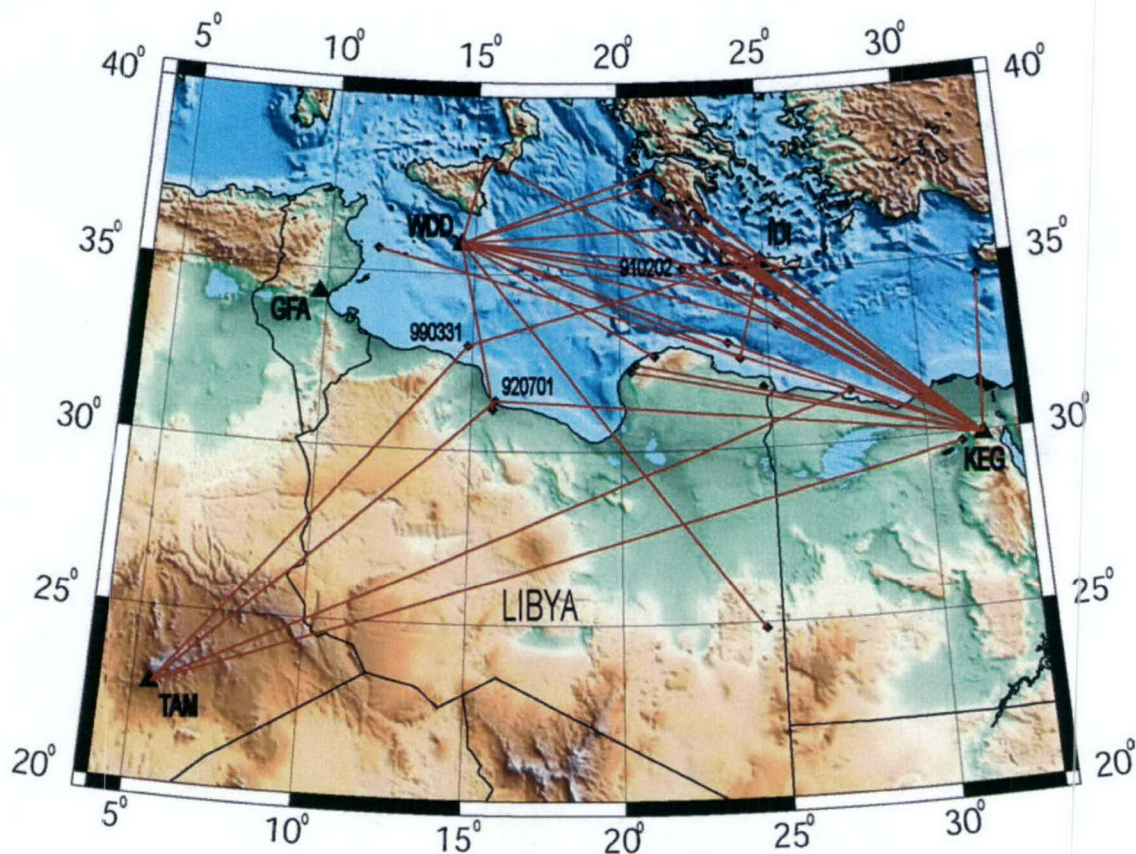


Figure 30. Map of study areas show earthquakes as black diamonds, stations as black triangles, and red great circle arcs represent source-receiver paths.

LIBYA3D Velocity Model

The LIBYA3D velocity model was derived from over 6000 gravity measurements, in conjunction with other geophysical and geological data obtained from oil exploration, published research, and other academic institutions to develop a 3D density model for the Libya region (Brown et al., 2004). The 3-D velocity model, LIBYA3D was derived from this density model. The model consists of 5 lithospheric layers reflecting the geology at depth, which includes Cenozoic/Mesozoic, and Paleozoic sedimentary layers overlying a Precambrian basement. An extra layer was added to account for the Mediterranean Sea. In the Libya region, the crust thins towards the north, and thus the model features a varying crustal thickness as determined from Dial (1998) (Figure 31). Overall the resulting velocity/density model shows a good correlation with the IASPEI91 model in P- and S-wave velocity and density (Kennett *et al.*, 1991). The major differences between IASPEI91 and LIBYA3D model lie on a localized scale.

Table 5. Earthquake Source Parameters (International Seismic Centre)

Date	Time	Lat.	Lon.	Dep.	mb
2000/05/21	22:45:38.3	31.1570	15.7340	23.6	3.8
1990/05/18	18:27:51.2	31.7130	24.7960	10.0	4.3
1990/05/25	15:44:45.9	37.8702	21.0578	1.0	3.8
1990/07/30	17:52:37.9	34.4845	25.5438	45.8	4.4
1991/02/02	05:34:47.3	35.1190	22.1571	10.0	3.7
1991/02/08	13:50:40.1	35.2852	23.0458	63.8	4.4
1991/05/28	18:58:46.6	37.0235	22.4817	20.8	4.5
1991/08/08	22:46:10.9	35.6467	11.6387	22.0	4.7
1992/07/01	15:13:32.8	31.4246	15.8143	10.0	4.2
1992/10/12	13:09:55.4	29.7566	31.1360	21.5	5.8
1993/09/09	00:32:35.5	32.2394	20.3859	10.0	4.8
1995/07/22	06:24:45.5	34.7502	23.3754	72.2	4.1
1995/08/02	01:42:20.6	33.4384	25.3153	33.0	3.4
1995/08/27	19:42:14.7	38.2610	15.2912	25.2	3.6
1995/11/25	14:10:46.0	28.8123	34.9227	14.0	3.8
1996/01/06	10:38:23.9	32.9867	23.6555	1.0	
1996/03/23	20:40:46.9	36.9910	21.8653	30.3	3.5
1996/05/19	14:15:14.2	34.1160	25.3398	37.6	4.0
1996/06/21	13:03:38.5	37.8847	21.2394	91.1	3.5
1996/10/09	16:57:40.1	36.8145	21.2931	13.6	4.0
1996/10/09	17:01:49.0	34.4148	32.1809	50.2	4.1
1996/10/30	10:43:02.9	32.4343	20.5326	10.0	4.6
1997/02/01	23:08:36.0	35.0318	24.4391	10.0	3.9
1997/05/10	14:03:03.6	24.8180	24.4750	0.0	3.9
1998/01/13	12:34:21.1	37.3992	20.7101	15.1	3.6
1998/04/12	22:06:31.0	37.4186	20.7159	10.0	4.4
1998/05/28	18:33:28.4	31.4459	27.6426	10.0	5.5
1998/08/08	16:39:28.7	36.2939	22.7695	5.0	3.5
1999/03/31	09:42:16.1	32.9550	14.8380	32.2	4.3
1999/06/17	10:18:02.2	32.5410	24.0530	10.0	4.3
1999/11/07	14:43:36.0	32.6600	21.1740	10.0	4.4

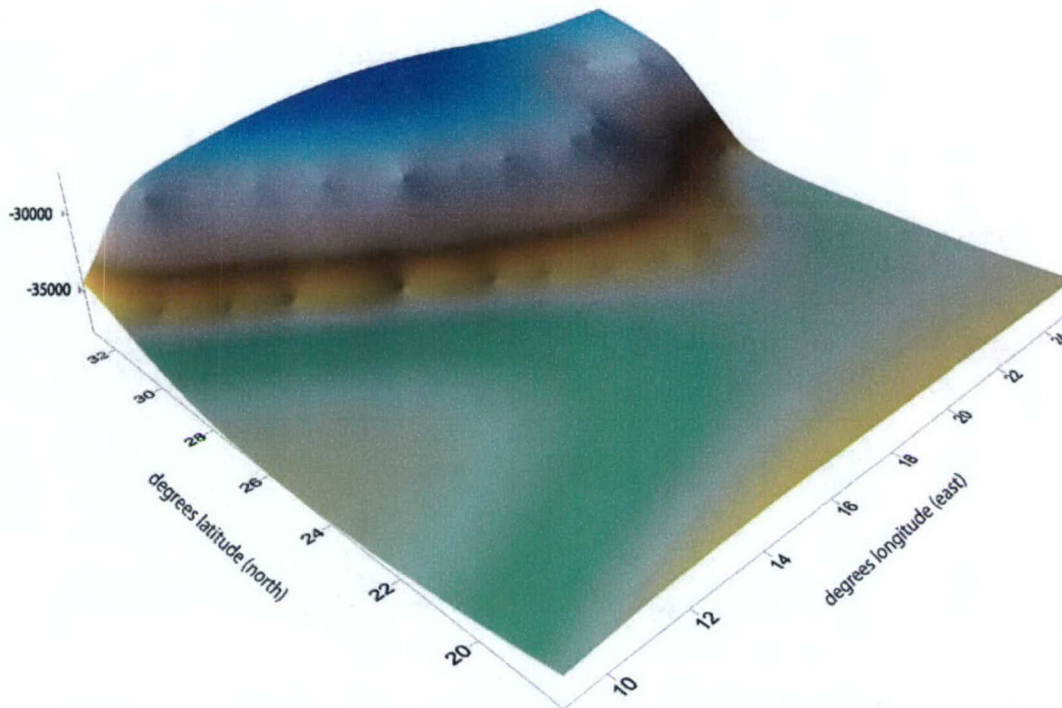


Figure 31. A portion of the LIBYA3D Moho boundary DEM used in our study showing crustal thickness under Libya, note the thinning crust to the north as Libya approaches the Mediterranean Sea.

Regional Seismic Data

We gathered seismic data for events that occurred from 18 May 1990 to 21 May 2000 in the Libyan region and the adjacent Mediterranean Sea. Event times and locations were obtained from the International Seismic Centre (ISC). We have data consisting of 31 natural events, 7 located in Libya, 1 located in Egypt, with the remainder located in the adjacent area of the Mediterranean Sea. Magnitudes range from (m_b) 3.7 to 5.7.

Waveform data were acquired from the Incorporated Research Institutions for Seismology's (IRIS) Data Management Center (DMC). The stations used in this research effort are Kottamia, Egypt (KEG), Wield Dalam, Malta (WDD), Tamanrasset, Algeria (TAM), Anoyia, Crete (IDI), and Gafsa, Tunisia (GFA), all with broadband instrumentation. We remove instrument response and set origin times for each event. Waveform data are then cut and rotated to their radial and transverse components, and finally, we apply a Butterworth filter to view the waveforms at several frequency ranges (0.5-1, 1-2, 2-4, 4-6, and 6-8 Hz) (Figure 32). We then pick regional phases P_n and S_n manually and mark the header for each waveform.

We show the 02 February 1991 (910202) event (Figure 32) recorded at KEG ($\Delta = 9.67^\circ$; $AZ = 120^\circ$) (see Figure 1); note the dramatic increase in SNR at the higher frequencies. This led us to investigate attenuation effects of source-receiver paths as related to their orientation across the varying topography and bathymetry of Libya and the Mediterranean Sea. Plotting all

seismograms at KEG and TAM for regional events shows consistent high frequency propagation of *Pn* and *Sn* energy at KEG and low frequency propagation of *Pn* and *Sn* energy at TAM.

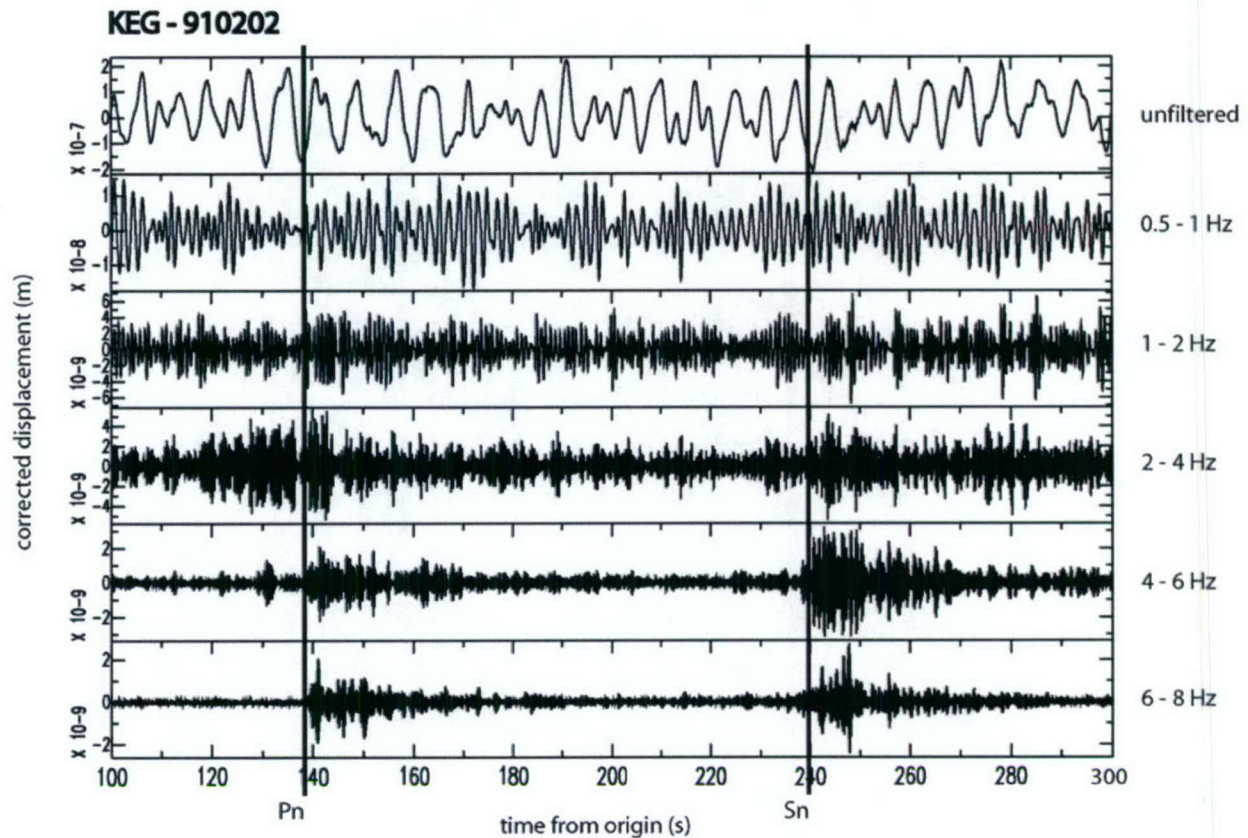


Figure 32. Vertical component multi-frequency bandpassed seismogram of the 02 February 1991 event recorded at KEG. Note that SNR increases at the higher frequency ranges. This is a good example that led us to question what path effects were responsible for the observed high frequency propagation.

Two events of particular interest, due to the fact they were recorded at two receivers, are the 31 March 1999 (990331) event recorded at IDI ($\Delta = 8.66^\circ$; $AZ = 71.9^\circ$) and TAM ($\Delta = 13.1^\circ$; $AZ = 221^\circ$), and the 01 July 1992 (920701) event recorded at KEG ($\Delta = 13.9^\circ$; $AZ = 92.0^\circ$) and TAM ($\Delta = 12.6^\circ$; $AZ = 229^\circ$) (Figure 33) (see Figure 30). The SNR for both events at TAM is low, from 4 to 8 Hz; however at IDI and KEG the SNR is still larger, if not dominant, from 4 to 8 Hz. Note the receiver distance to KEG is greater than the receiver distance to TAM for 920701 (Figure 33B), but the SNR is still strong enough to be seen at KEG in the high frequency ranges. This demonstrates that receiver distance is not the primary controlling parameter for signal attenuation.

We calculate phase amplitude and signal to noise ratio (SNR) by measuring the maximum displacement in a ten second pre-phase and phase window. By comparing the SNR of *Pn* against frequency at a specific station (Figure 34A-C) we observe trends in station-frequency

dependence. These trends were normalized by dividing each point by the SNR at the lowest frequency range for each event (0.5-1.0 Hz). This highlights the difference in high frequency propagation. As seen in these diagrams, KEG conveys the most dramatic results with the SNR peaking at 6-8 Hz in 10 of the 14 events recorded there. IDI and WDD show a trend similar to KEG with good SNR at 4 to 8 Hz, but they actually peak at 3 Hz for most of these Intra-Mediterranean events. We combine their results due to their similar trends, as well as the fact that their receiver environments are the same topographically. TAM shows expected high frequency attenuation of Pn energy.

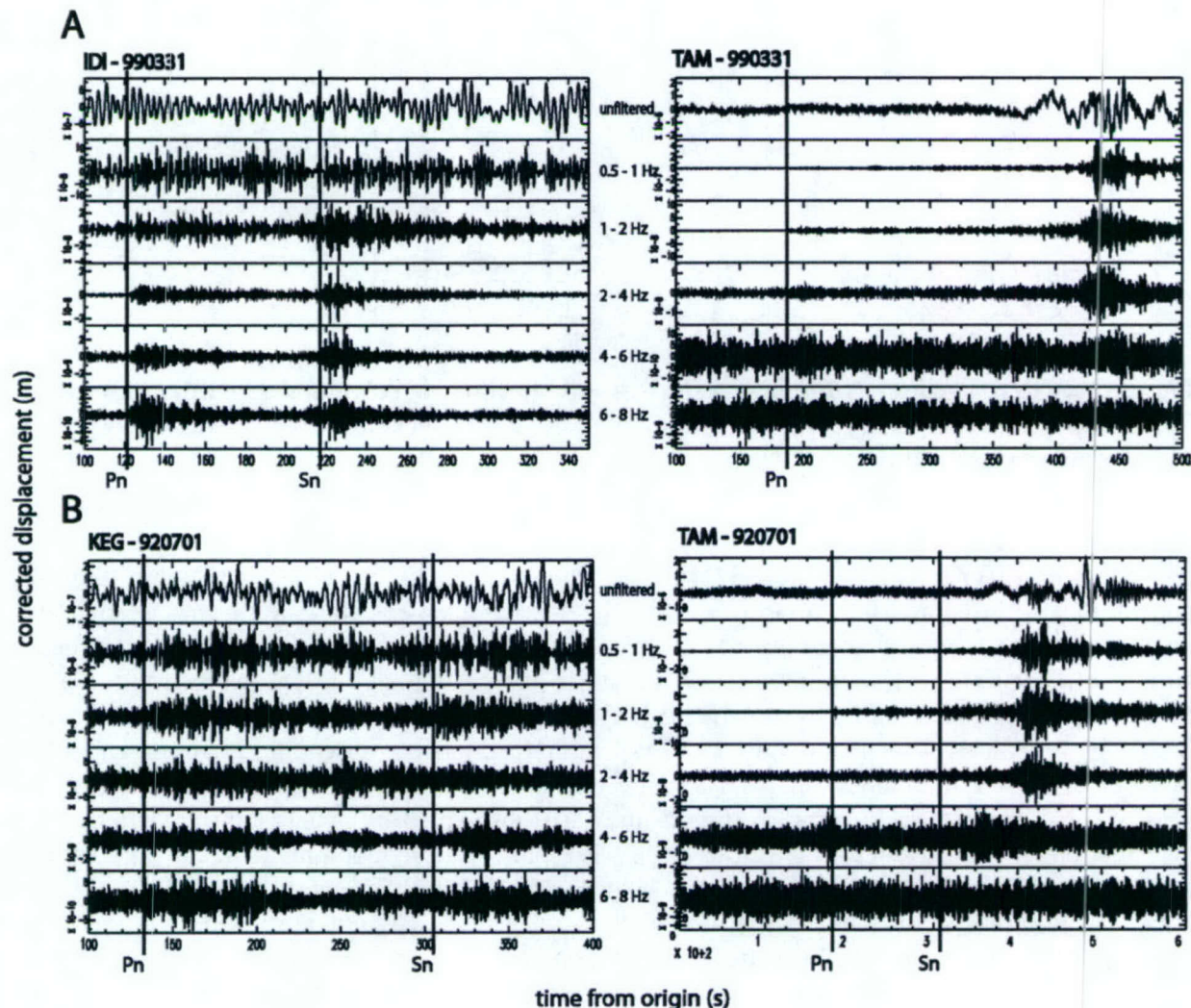


Figure 33. Vertical component multi-frequency seismograms from the 990331 and 920701 events. Notice the different high-frequency propagation when comparing IDI and KEG to TAM. Also note that even though the receiver distance is greater to KEG than to TAM for 920701 a distinguishable signal is still present from 4 to 8 Hz at KEG.

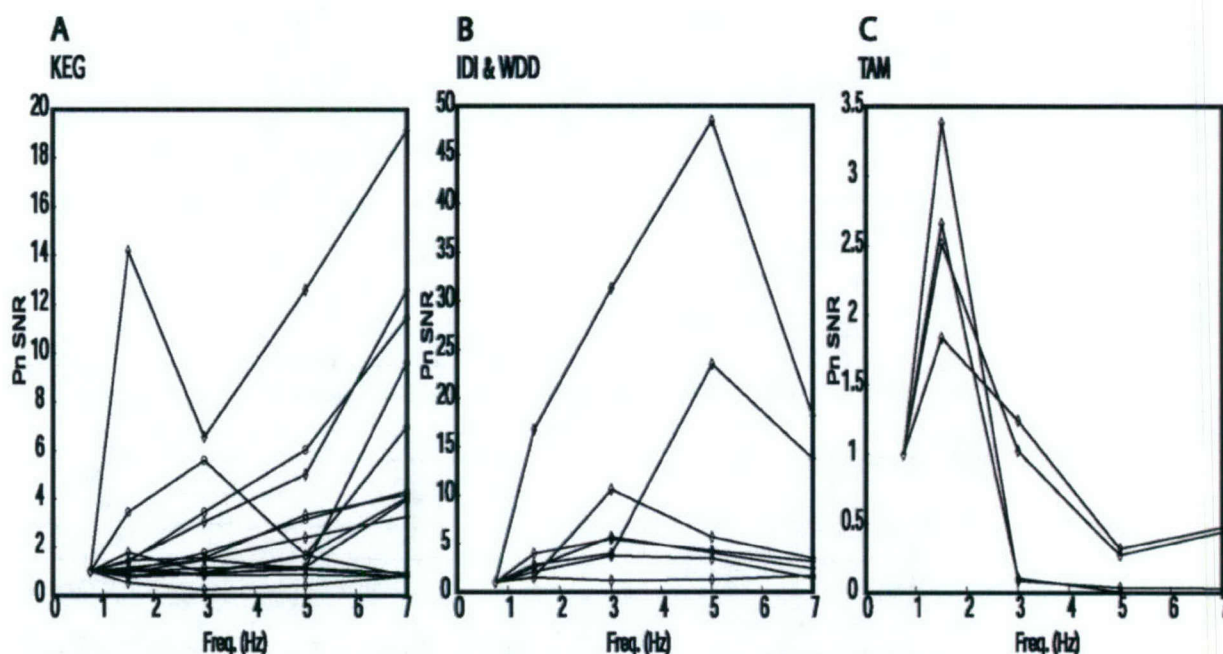


Figure 34. SNR-Frequency diagrams show trends in station-frequency dependence, note the unusual high frequency propagation displayed at KEG accompanied by the expected high frequency attenuation at TAM.

Application of LIBYA3D

Using LIBYA3D (see Figure 31) we were able to calculate variable topographic statistics concerning the crust and the Moho related to the source-receiver paths. With the use of a 0.5 degree wide swath, we calculate the crustal volume for each source-receiver path. We also use a simple, but accurate map measurement to determine the percentage of continental crust in each source-receiver path. Finally, using LIBYA3D we calculate the standard deviation of the Moho, which is similar to Zhang and Lay's (1994) surface roughness calculation, of each source-receiver path. We then calculate the cross-spectral amplitude and cross-spectral SNR values of P_n (1-2 / 6-8 Hz) for each event; in this fashion, we can define the events with high-frequency propagation by their low cross-spectral value. We plot these topographic statistics against the cross-spectral values and seek correlations (Figure 35A-F) (e.g., Zhang & Lay, 1994). Due to the small amount of data that we have to work with for each plot we define a correlation coefficient (r) greater than 0.5 as a strong correlation.

At KEG, we find correlations between high frequency propagation and the percentage of continental crust in the source-receiver path when compared to cross-spectral amplitude and cross-spectral SNR (Figure 35A, B) and a weak correlation between high frequency propagation and crustal volume. For IDI, WDD, and TAM there are strong correlations when comparing percentage of continental crust and crustal volume to cross-spectral SNR (Figure 35C, D). However, these correlations break down when compared to cross-spectral amplitude. Finally, we find two distinct correlations at KEG for standard deviation of the Moho (Figure 35E, F). When compared to cross-spectral SNR a positive slope is exhibited, however, when compared to cross-spectral amplitude a negative slope is produced.

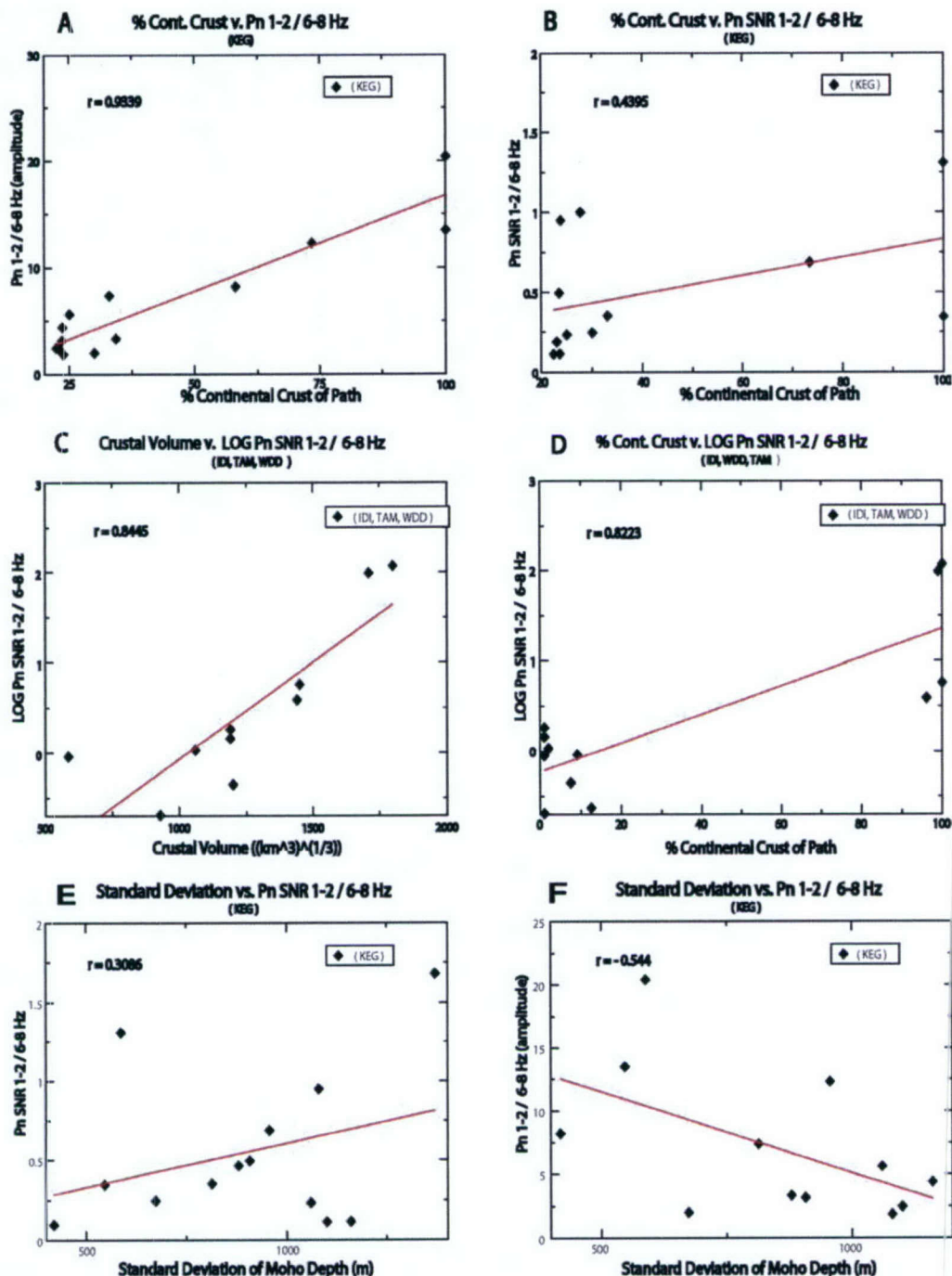


Figure 35. Cross-spectral value plots show a good correlation between the continental crust percentage in the source-receiver path and cross-spectral values at KEG (A & B). Strong correlations are also shown for IDI, TAM, and WDD when compared to crustal volume and continental crust percentage (C & D). Finally, we observe converse trends at KEG when compared to the standard deviation of the Moho depth (E & F).

Discussion

A 3-D velocity model can aid in improving discrimination between earthquakes and explosions by providing a means for determining the contributing factors in regional wave propagation. Formal approaches to regional waveform propagation, such as Magnitude Distance and Amplitude Corrections (MDAC) (Taylor et al., 2002) rely on developing magnitude and amplitude corrections based on empirical data at various frequencies. However, when few events exist due to the nature of the tectonic region, these empirical based approaches break down. Utilizing a 3D model developed using other geophysical data may be the only means to correct for high frequency regional propagation. Although we do not formally develop corrections, we can extend this application of the model to develop crustal path corrections to high frequency propagation.

We see through our various geophysical plots that there are several parameters that affect amplitude and SNR at varying frequencies for a particular phase, in our case, P_n . By having all of our plots dependent on the same cross-spectral values we can empirically gauge which parameters have the greatest effect on these values. We identify a strong correlation between percentage of continental crust and cross-spectral SNR at KEG. More importantly, the correlations between crustal volume and Moho standard deviation with cross spectral values not only show solid parameters for future correction and verification work, but also serve to validate the LIBYA3D model.

We recognize that these correlations are not perfect, but nature rarely exhibits such perfect fits. This leads us to further examine outlying events in our plots. We see that high frequency propagation is most stringently controlled by the percentage of continental crust in the source-receiver path, which relates to the crustal volume. Secondly, standard deviation (roughness) of the Moho boundary influences high frequency propagation. We also see that other source parameters such as depth, magnitude, and finally distance all play a hand in controlling the high-frequency propagation of P_n . Since we know that velocity gradients above and below the Moho trap seismic energy resulting in larger P_n amplitudes (Stein & Wysession, 2003) and it has been shown that P_n attenuates less rapidly at higher frequencies if the spherical earth velocity gradient is zero or greater (Sereno & Givens, 1990); we feel that this is also a parameter controlling high frequency propagation in our events.

Conclusions

By performing a multi-frequency analysis, we find that P_n and S_n show stronger amplitudes at higher frequencies (4 – 8 Hz) along propagation paths where continental crust is limited. Conversely, we only observe strong P_n and S_n amplitudes at lower frequencies (0.5 – 4 Hz) along propagation paths where continental crust is prevalent. We discover that at regional station KEG, we see a strong correlation between percentage of continental crust and signal propagation in the high frequency ranges, and this relationship persists as well for IDI, WDD, and TAM, even though there is a lack of data. Most of the paths for IDI and WDD are purely oceanic, since they are island stations, while the paths for TAM are purely continental, which skews the results. We feel that given a full range of data this parameter will consistently predict high frequency propagation events that would aid in verification work in regions of mixed crusts. Using LIBYA3D, we found correlations for all four stations when comparing crustal volumes to cross-spectral values. We feel more data are needed before drawing any solid conclusions on the relationship between crustal volume and high frequency propagation.

We find interesting results at KEG when comparing cross-spectral values against the standard deviation (roughness) of the Moho. We see that greater roughness degrades the SNR at higher frequencies (4-8 Hz), but simultaneously causes less rapid attenuation at these higher frequencies. We question if there is a link between roughness of the Moho and its velocity gradient, which is known to increase the amplitude of the P_n phase. Finally, we conclude that 3-D geophysical models such as LIBYA3D are valuable for conducting regional amplitude correction and verification work in regions where little or no explosion data are available. This becomes even more important since this is the case for many stations currently monitoring the Comprehensive Test Ban Treaty (CTBT).

REFERENCES

- Afek, Y., and Brand, A., 1998. Mosaicking of orthorectified aerial images, *Photogrammetric Engineering & Remote Sensing*, **64**, 115-125.
- Baker M.R., 2001. SURFGRAV, user's guide. 9 pp.
- Blanco, M. J., and Spakman, W., 1993, The p-wave velocity structure of the mantle below the Iberian Peninsula: Evidence for subducted lithosphere below southern Spain, In: Badal, J., Gallart, J. and H. Paulssen (Eds.), *Seismic studies of the Iberian Peninsula, Tectonophysics*, **221**, 13-34.
- Bott, M. P., 1959. The use of electronic digital computers for the evaluation of gravimetric terrain corrections: *Geophys. Prosp.*, **7**, 45-54.
- Brown, W. A., and Doser, D.I., Keller, G. R., and Velasco A. A., (in preparation) The use of Free Air gravity data to constrain 3D density model for the Libya region. *J. Geophys. Res.*,
- Budding, A. J., 1978. Gravity survey of the Pajarito Plateau, Los Alamos and Santa Fe Counties, New Mexico, *Los Alamos National Laboratory Report LA- 7419-MS*, 15.
- Campbell, A. S., 1968. The Barce (Al Marj) earthquake of 1963. Geology and Archeology of Northern Cyrenaica, Libya (ed. F. T. Barr). *Petrol. Explor. Soc. Libya*, 10th Annu. Field Conf., 183-195.
- Carmichael, R. S., 1989. *Practical Handbook of Physical Properties of Rocks and Minerals*, CRC Pres, Inc. 741pp.
- Crotwell, H. P., Owens, T. J., Ritsema, J., 2000. The TauP toolkit: Flexible seismic travel time and ray path utilities. *User Guide*.
- Dial, P., 1998. An integrated geophysical study of north Africa and Mediterranean lithospheric structure, *Ph.D. Dissertation*, University of Texas at El paso, 207 pp.
- ENVI User's Guide, 1998. Research System, Inc. 930pp.
- Eros (Earth Resources Observation Systems), Data Center (EDC), 1996. GTOPO30 (a Digital Elevation Model), United states Geological Survey (USGS), www.usgs.gov.
- Ferguson, J. E., W.S. Baldrige, L. W. Braile, S. Biehler, B. Gilpin and G. R. Jiracek, 1995. Structure of the Espanola Basin, Rio Grande rift, New Mexico, from SAGE seismic and gravity data, *Geology of the Santa Fe Region, New Mexico Geological Society Guide book*, **46**, 105-110.
- Genik, G. J., 1992. Regional framework, structural and petroleum aspects of rift basins in Niger, Chad, and the C.A.R., In: Zeigler, P. A. (Ed.), *Geodynamics of Rifting*, Vol. II, Case studies on rifts: North and South America and Africa, *Tectonophysics*, **213**, 169-185.
- Gitterman, Y. Pinsky V. and Shapira, A., 2003. Improvements in monitoring the CTBT in the Middle East by the Isreal seismic network. *Technical report, prepared for DTRA*, October, 2003. 177pp.
- Goldstein, P., Dodge, D., Firpo, M., 1999. "SAC2000": Signal processing and analysis tools for seismologists and engineers, UCRL-JC-135963, Invited contribution to the *IASPEI International Handbook of Earthquake and Engineering Seismology*.
- Goudarzi, G.H., 1980. Structural-Libya, in M. T. Busrewill, editors.: *The geology of Libya, volume III: London, Academic Press*, 879-892p.
- Goudarzi, G.H, and Smith J.P., 1978, Preliminary-structure contour map of the Libyan

- Arab Republic and other adjacent areas, *USGS. Map I-350 A*, scale 1:2,000,000.
- Goudarzi, G.H, 1970. Geology and mineral resources of Libya – A reconnaissance : *U. S. Geological survey Professional Paper 660*, 104 pp.
- Ghuma, M. A., and Rogers, J. J., 1978. Geology, Geochemistry and, tectonic settings of the Ben Ghnema Batholith, Tibesti massif, Southern Libya, *GSA Bulletin*, **89**, 1351-1358.
- Gumper, F., and Pomeroy, P. W., 1970, Seismic wave velocities and Earth structure on the African continent, *Bull. Seis. Soc. Am.*, **60(2)**, 651-668.
- Gutenberg, B. and Richter, C. F., 1965. Seismicity of the earth and associated phenomena in the Alpine Belt, *Geol. Soc. Am.* **57**, no.12, Part 2, 1253pp.
- Hallet D., 2002. Petroleum Geology of Libya, *Elsevier Science B.V.* 503 pp.
- Hammer, S., 1939. Terrain correction for gravimeter stations: *Geophysics*, **4**, 184-194.
- Hammuda, O. S., 1980. Geologic factors controlling fluid trapping and anomalous fresh water occurrence in the Tadrart sandstone, Al Hamada Al Hamra area, Ghadamis Basin, Libya, in M. J. Salem and M.T. Busrewill, eds., (*The Geology of Libya, volume II*): London, Academic Press, 501-507p.
- Hansen, M., Anandan, P., Dana, K., van der Wal, G., and Burt, P., 1994., Real-time scene stabilization and mosaic construction *IEEE Workshop on Applications of Computer Vision*. December, Florida, 54-62.
- Hayford, J. F., Bowie, W., 1912. The effect of topography and Isostatic compensation upon the intensity of gravity: *Special Publ. 10 U.S. Coast and Geodetic Surv.*
- Hearn, P. Jr., Hare, T., Schruben, P., Sherill, D., LaMar, C., and Tsushima, P., 2001. Global GIS Database: Digital Atlas of Africa, *USGS. Digital Data Series (DDS-62-B)*.
- Irani, M., Anandan, P., and Hsu, S., 1995a. Mosaicked based representations of video sequences and their applications, *Proceedings of the 5th international conference on computer vision*. June, Cambridge, MA, 605-611pp.
- Irani, M., Hsu, S., and Anandan, P., 1995b. Video compression using mosaic representations. *Signal Process. : Image Commun.* **5 (30)**, 529-552.
- Irani, M., and Anandan, P., 1998. Video indexing based on mosaic representations. *Proc. IEEE* **86 (5)**, 905-921.
- Johnson, M. and Vincent, C., 2002. Development and testing of a 3D velocity model for improved Event Location: A case study for the India-Pakistan region, *Bull. Seismo. Soc Am.*, **92**, no. 8, 2893-2910.
- Kane, M. F., 1962. A comprehensive system of terrain correction using a digital computer: *Geophysics*, **27**, 455-462.
- Kebeasy, R. M., 1980. Seismicity and Seismotectonics of Libya, *Second Symposium on the geology of Libya*. (eds. M.J. Salem, M.T. Busrewil), Academic Press, New York, **3**, 955-963.
- Kennett, B.L.N., and Engdahl, E.R., 1991. Travel times for global earthquake location and phase identification, *Geophys. J. Int.* **105**, 429-465.
- Kennett, B.L.N., 1983. *Seismic Wave Propagation in Stratified Media*, Cambridge University Press, Cambridge. 350pp.
- Khatun, S., 2003. A precision gravity study of the Southern Mesilla Bolson, West Texas, *M.S. Thesis*, University of Texas at El Paso, 87 pp.
- Kim, D., Yoon, Y., and Choi, J., 2003. An effective method to build panoramic image mosaics, *Pattern Recognition Letters*, **24**, 2421-2429.
- McNamara, D.E., Walter, W.R., Schultz, C. and Goldstein, 1996. Regional phase

- propagation in northern Africa and the Mediteranean (abstract), *Seism, Res. Lett.*, **67**, 47.
- Minami, K., 1963. Relocation and reconstruction of the town of Barce, Cyrenaica, Libya, damaged by the earthquake of 21, February 1963. *UNESCO*.
- Moik, J. G., 1980. Digital processing of remotely sensed images, *Nasa*.
- Mullen, R. R., 1980. Aerial mosaics and orthophotomaps, *Manual of photogrametry, Fourth Edition* (C. C Slama, editors), American Society of Photogrametry, Falls Church, Virginia, 761-783.
- Nafe, J. E., and Drake, C. L., 1957. Variation with depth in shallow and deep water marine sediments of porosity, density and the velocities of compressional and shear waves, *Geophysics*, **22**, 523-552.
- Nagy, D., 1966. The prism method of terrain corrections using digital computers: *Pure and appl. Geophys.*, **63**, 31-39.
- Pasyanos, M.E. and Walter, W.R., 2002. Crust and upper-mantle structure of North Africa, Europe and the Middle East from inversion of surface waves. *Geophysical Journal International*. **149**, 463-481.
- Pasyanos, M.E. Walter, W.R., and Hazler, S.E. 2001. A surface wave dispersion study of the Middle East and North Africa for monitoring the Comprehensive Nuclear-Test-ban Treaty, *Pageoph*, **158**, 1445-1474.
- Pegram, W. J., Register, J. K., Fullagar, P. D., Ghuma, M. A., and Rogers, J. J. W. 1976. Pan-African aes from Tibesti massif batholith, Southern Libya, *Earth Planet. Sci. Lett.*, **30**, 123-128.
- Piccoli, G., 1970. Outlines of volcanism in northern Tripolitania Africa. Proceedings of a joint meeting of the institute (Libya), *Boll. Soc. Geol. Ital.*, **89**, 449-461.
- Plouf, D., 1966, Digital terrain corrections based on geographic coordinates (abstract): *Geophysics*, **31**, 1208
- Plouf, D., 1977. Preliminary documentation for a FORTRAN program to compute gravity-terrain corrections based on topography digitized on a geographic grid: *US Geol. Surv. Open-file report*, 77-535.
- Qiu, X., Priestley, K. and McKenzie, 1996, Average lithospheric structure of southern Africa, *Geophys. J. Int.*, **127**, 563-587.
- Randall, G. R. Ammon, C. T., and Owens, 1995. Moment-tensor estimation using regional seismograms from a Tibetan Plateau portable network deployment, *Geophys. Res. Lett.* **22**, 1665-1668.
- Scheik, C. G., 2004. Terrain change detection using aster optical satellite imagery along the Kunlun fault, Tibet, *MS. Thesis*, University of Texas at El Paso, 107pp.
- Seber, D., Barazangi, M., Tadili, B.A., Ramdani, M., Ibenbrahim, A. and Sari, D.B., 1996. Three-dimensional upper mantle structure beneath the intraplate Atlas and interplate Rif Mountains of Morocco, *J. Geophys. Res.*, **100**, 3125-3138.
- Sereno, T. J. & Givens, J. W. 1990. Pn attenuation for a spherically symmetric Earth model, *Geophys. Res. Lett.* **17**, 1141-1144.
- Stein, S. & Wysession, M. 2003. An Introduction to Seismology, Earthquakes, and Earth structure. Malden: Blackwell Publishing.
- Suleiman, A. S., and Doser, D.I., 1995. The seismicity, seismotectonics and earthquake hazards of Libya with detailed analysis of the 1935 April 19, M = 7.1 earthquake sequence, *Geophys.J. Int.* **120**, 312-322.
- Suleiman, I. S., 1976. Petrographic and subsurface study of the Late Silurian Accacus

- sandstone, Tigi, Field, Northwestern Libya: Unpub. Postgr. Diploma in Geology, Univ. Tripoli, Libya, 87 pp.
- Suleiman, I. S., 1985. Gravity and heat flow studies in the Sirte Basin, Libya, *Ph.D. Dissertation*, University of Texas at El Paso, 186 pp.
- Suleiman, I.S., Keller, G.R., and Suleiman, A.S. 1991. Gravity study of the Sirt Basin, Libya. *Third Symposium on the geology of Libya. vol 6* (eds. M.J. Salem, A.M. Sbata and M.R. Bakbak), Elsevier, Amsterdam, 2461-2468.
- Szeliski, R., 1994. Image mosaicking for Tele-Reality applications, *IEEE Workshop on Applications of Computer Vision*. December, Florida, 44-53.
- Szeliski, R., 1996. Video mosaics for virtual environments. *IEEE Comput. Graph. Appl.*, 22-30.
- Szeliski, R., and Shum, H.Y., 1997. Creating full view panoramic image mosaics and environment maps, *Proceedings SIGGRAPH*. 251-258.
- Taylor, S. R., et al. (2002). Amplitude corrections for regional seismic discriminants, *Pure Appl. Geophys.* **159**, 623-650.
- Vachette, M., 1964. Ages radiométriques des formations cristallines d' Afrique équatoriale (Gabon, République Centrafricaine, Tchad, Moyen Congo). *Ann. Fac. Sci. Univ. Clermont*, **25**, 31 pp.
- VanDeMark, T. F., Brown, W. A., Doser, D. I., and Velasco, A. A., (submitted, 2004). Analysis of high frequency propagation in the Libya region utilizing a 3-D geophysical model. *Bull. Seismo. Soc. Am.*
- Veilleux, A. M., 1999. Shallow subsurface geophysics of the Pajarito plateau, New Mexico. *M.S. Thesis*, University of Texas at El Paso, 90 pp.
- Velasco, A. A., Hartse, H. E., & Randall, G. E. (2003). Propagation or source? Analysis of a moderate-magnitude seismic event in the Qinghai Province, China, *Bull. Seism. Soc. Am.* **93**, 2281-2288.
- Vickers, E. W., 1993. Production procedures for an oversized Satellite image map, *Photogrammetric Engineering & Remote Sensing*, **59**, 247-254.
- Walter, W. R., Mayeda, K. M., & Patton, H. J. (1995). Phase and spectral ratio discrimination between NTS earthquakes and explosions. Part I: Empirical observations, *Bull. Seism. Soc. Am.* **85**, 1050-1067.
- Xie, H., 2002, Application of integrated remote sensing and GIS technologies to Geological Agricultural, Water and Environmental issues in far west Texas. *PhD. Dissertation*, University of Texas at El Paso, 248 pp.
- Yousef, A. A., 1986, A surface wave dispersion study of the lithospheric structure of Africa, *Ph.D. Dissertation*, University of Texas at El Paso, 115 pp.
- Zhang, T. & Lay, T. (1994). Analysis of short-period regional phase path effects associated with topography in Eurasia, *Bull. Seism. Soc. Am.* **84**, 119-132.
- Zhou, X., Zhong, B., Li, X., 1990. Gravimetric terrain corrections by triangular-element method: *Geophysics*, **55**. 232-238.